

ANALYSIS OF GPR DATA FOR TIME AND FREQUENCY-DEPENDENT EFFECTS OF  
CHANGING WATER TABLE LEVELS

by

Samuel Kwaku Amankwaa



APPROVED BY SUPERVISORY COMMITTEE:

---

George A. McMechan, Chair

---

William R. Griffin

---

Tom H. Briskowski

Copyright 2019

Samuel Kwaku Amankwaa

All Rights Reserved

I dedicate this work to my parents Mr. and Mrs. Amankwaa, all my siblings and my future wife  
and unborn kids.

ANALYSIS OF GPR DATA FOR TIME AND FREQUENCY-DEPENDENT EFFECTS OF  
CHANGING WATER TABLE LEVELS

by

SAMUEL KWAKU AMANKWAA, BS

THESIS

Presented to the Faculty of  
The University of Texas at Dallas  
in Partial Fulfillment  
of the Requirements  
for the Degree of

MASTER OF SCIENCE IN  
GEOSCIENCES

THE UNIVERSITY OF TEXAS AT DALLAS

May 2019

## ACKNOWLEDGMENTS

My sincere appreciation goes to my supervisor, Prof. George McMechan for giving me the opportunity to work with him. I would like to thank him for every experience I have gained by working with him. This research would have been impossible without his guidance, patience and excellent ideas. I am especially grateful to him for providing me with all the previously collected data from 1998 to 2017 as well as providing the software used in the processing and interpretation of the data. Special acknowledgement is given to all past students of UTD GPR classes from 1998 to 2017 for their role in collecting all the previous data. Thank you to my supervisory committee members Dr. Randy Griffin and Dr. Tom Brikowski for their help throughout this research.

Thank you to my UTD Geosciences professors for inspiring me to be a geoscientist and ultimately pursue a graduate degree in Geosciences. I also want to thank Geosciences Department staff members Gloria Eby and Kyong Edwards. I wish to express my gratitude to all members and staff of the UTD Geophysical Consortium and the Center for Lithospheric Studies especially, Sharon Edwards, Chen Tang and Sasmita Mohapatra for their individual and collective support over the past one and a half years. It was a great privilege to use GPR instruments and computers in the Center for Lithospheric Studies to facilitate my research. I am thankful to all my friends at The University of Texas at Dallas, especially Chiamaka Oyekwe, Ozo Gladsome, Micheal Anekwe and Solomon Akatakpo.

I would also like to thank my family, particularly my mother, Mrs. Theresah Afia Fofie and my sister, Mrs. Mary Fosuhemaa for their moral support and encouragement to pursue higher academic achievements.

April 2019

# ANALYSIS OF GPR DATA FOR TIME AND FREQUENCY-DEPENDENT EFFECTS OF CHANGING WATER TABLE LEVELS

Samuel Kwaku Amankwaa, MS  
The University of Texas at Dallas, 2019

Supervising Professor: George A. McMechan

Frequency-dependent ground-penetrating radar (GPR) data are acquired every 2-3 years from 1998 to 2017 at a single location on an exposure of the Lewisville Member of the Woodbine Formation along the shore of Grapevine Lake in North Texas. The depth to the groundwater in the outcrop varies in position with the water level in the lake, and the short-term rainfall history. Thus, the distribution of fresh and ground water and their different dielectric permittivities and electrical conductivities produce visible time and frequency-dependent GPR velocities and attenuations. The lithologic interbedding of sands and thin clays, the presence of fractures, and the distribution of hematite in the uppermost layer, and a shallow unconformity, all contribute to variations in GPR amplitude and attenuation. The difference between the known minimum and maximum water table levels of  $\sim 3.38$  m is consistent with observed changes in GPR velocity from  $\sim 0.063$  m/ns to  $\sim 0.52$  m/ns, and with the observed difference of 31.9 cm of rainfall and an average porosity of 20%. The presence of hematite in the near-surface part of the section attenuates the GPR signals and produces an amplitude variability of a factor of  $\sim 3$ .

## TABLE OF CONTENTS

ACKNOWLEDGMENTS.....	v
ABSTRACT.....	vi
LIST OF FIGURES.....	ix
LIST OF TABLES.....	xii
CHAPTER 1 INTRODUCTION.....	1
1.1 Geology of the study area.....	2
CHAPTER 2 METHODOLOGY.....	9
2.1 GPR Method.....	9
2.2 Research Objectives.....	10
2.3 Data acquisition and field work.....	10
2.4 Data processing and analysis.....	14
2.4.1 GPR data processing.....	16
2.4.2 Velocity analysis.....	17
2.4.3 Comparing velocity models at different lake levels.....	18
2.4.4 2D Pre-stack Kirchhoff migration.....	19
2.4.4.1 2D velocity grid.....	19
2.4.4.2 2D ray tracing and two-way time map construction.....	21
2.4.4.3 Migration.....	21
CHAPTER 3 RESULTS AND INTERPRETATIONS.....	23
3.1 Subsurface geological features.....	23
3.2. Analysis of 2D GPR data with respect to water table position.....	25

3.2.1	Analysis of 2D models as a function of fresh and ground water distribution.....	28
3.2.1.1	Control of fresh and lake water distribution and visibility of GPR reflections by porosity.....	31
3.2.2	Repeatability of data from years with small differences in lake level.....	33
3.3	Sensitivity of GPR to ironstone beds.....	34
CHAPTER 4 DISCUSSION AND CONCLUSIONS.....		36
4.1	Discussion.....	36
4.2	Conclusions.....	37
APPENDIX A TIME TO DEPTH CONVERSION.....		38
APPENDIX B ESTIMATION OF ROCK POROSITY.....		39
APPENDIX C GOVERNING EQUATION OF GPR VELOCITY.....		40
APPENDIX D 2D PROFILE IMAGES OF GPR DATA FROM OTHER YEARS.....		41
REFERENCES.....		44
BIOGRAPHICAL SKETCH.....		48
CURRICULUM VITAE		



## LIST OF FIGURES

Figure 1. Stratigraphy of the Woodbine Formation. The green arrow shows study location.....	3
Figure 2. Map showing the study location along the north side of Grapevine Lake.....	4
Figure 3. Location of GPR Survey Line along Grapevine Lake.....	5
Figure 4. Red ironstone-cemented pebbly conglomerate with concretions at the top of Unit 7.....	7
Figure 5. Exposed cliff face showing lithologic units. Tidal channel sandstones grading upwards into rippled flaggy bedded tidal flat sandstones at Fishing Trail 2 section, Murrell Park.....	7
Figure 6. Lithologic Unit 3. Fine grained moderately well sorted sandstone showing small scale trough cross-stratification and straight crested ripples at the top.....	8
Figure 7. Main components of a ground penetrating radar system.....	12
Figure 8. Sensors & Software® 100 MHz transmitter and receiver combination ready for data collection.....	13
Figure 9. (a) Rod and (b) tripod-mounted level and for measuring water level and Topography.....	13
Figure 10. Tape measure on the ground showing the 50 m long survey line.....	14
Figure 11. Flow chart for GPR Data collection, filtering/processing and analysis.....	15
Figure 12. Plot of lake elevations against data acquisition years.....	16
Figure 13. Plot of 2017 and 2014 50 MHz RMS velocity curves superimposed on the 2014 time data. 2014 (the green curve) has velocities ranging from 0.13 m/ns to 0.76 m/ns corresponding to the low water content. 2017 (the orange curve) has the highest recorded water level with highly saturated rocks slowing down GPR velocities to ranges from 0.116 m/ns to 0.68 m/ns.....	19
Figure 14. Interval velocity-depth plot showing the 50 MHz velocity curves of 2017, 2014, 2011 and 2008 superimposed on the lithologic units. The 2014 data (black curve) shows maximum velocity while 2017 (red curve) has the least	

velocity at most depths. 2011 and 2008 (blue and pink curves) have intermediate velocities with values that lie between those of 2014 and 2017.....	20
Figure 15. (a) 2017 and (b) 2014 50 MHz profiles after dewowing and time alignment. Oval circles enclose incoherent areas at the left-hand side of each profile.....	21
Figure 16. (a) 2017 50 MHz profile and (b) 2014 50 MHz profile after Kirchhoff migration using the measured topography as the datum.....	23
Figure 17. 50 MHz, 100 MHz and 200 MHz matrix and wiggle profile plots of 2014 (a, d and g), 2005 (b, e and h) and 2017 (c, f and i) data showing the water table, level of attenuation and subsurface geologic features. All 50 MHz data (a), (b) and (C) are plotted to a maximum depth of 13 m, 100 MHz to a maximum depth of 9 m and the 200 MHz to a maximum depth of 6.1 m. Traces are sampled at 0.125 m. Solid vertical black lines represent the true depth of the cliff face measured from the surface. Black arrows show the water level of each survey year such as 2014 ~6.59 m, 2005 ~4.42 m and 2017~3.36 m, Ovals show regions of large recorded amplitudes caused by the erosion of the ironstone beds at both ends of the cliff face. The uppermost thin yellow line in each one of them is the free surface topography. Plotted depths are relative to the highest elevation on the line, at ~12 m, not relative to the topography. The solid black vertical line is the reference location relative to the center of the CMP mark. This is where the velocity profiles of Figure 14 are determined.....	27
Figure 18. Cumulative precipitation of 2005, 2014 and 2017 prior to the day of GPR data collection. Of these 3 years, the least amount of rainfall 42.7 cm was recorded in 2014. 2005 had 48.53 cm; 2017 had 74.6 cm. All precipitation data are converted from inches to cm.....	29
Figure 19. 50MHz, 100 MHz and 200 MHz matrix and wiggle profile plots of 2008 (a, c and e) and 2011(b, d and f) data showing the water table, the strength of attenuation and subsurface geologic features. All 50 MHz data (a and b) are plotted to a maximum depth of 13 m, 100 MHz (c and b) to a maximum depth of 9 m and the 200 MHz (e & f) to a maximum depth of 6.1 m. Traces are sampled at 0.125 m. Arrows show the water level of each year such as 2008 ~ 4.81m and 2011~ 4.46 m. Ovals show regions of large recorded amplitudes caused by the erosion of ironstone beds at both ends of the cliff face. The uppermost thin yellow line in each figure is the free surface topography. Plotted depths are relative to the highest elevation on the line, at ~12 m, not relative to the topography. The solid black vertical line is the reference location relative to the center of the CMP mark. This is where the velocity profiles of Figure 14 are determined.....	32
Figure 20. Hand sample of an ironstone concretion from Unit 7. The dominant mineral is hematite which exhibits strong attenuation of electromagnetic waves.....	35

Figure 21. (a) 50MHz, (b) 100 MHz and (c) 200 MHz matrix and wiggle profile plots of 1998 data showing the strength of attenuation and subsurface geologic features. 50 MHz data (a) is plotted to a maximum depth of 13 m, 100 MHz (b) to a maximum depth of 9 m and the 200 MHz (c) to a maximum depth of 6.1 m. Traces are sampled at 0.125 m. Lake elevation at the time of data collection is 161.7 m. The uppermost thin yellow line in each figure is the free surface topography. Plotted depths are relative to the highest elevation on the line, at ~12 m, not relative to the topography.....41

Figure 22. (a) 50MHz, (b) 100 MHz and (c) 200 MHz matrix and wiggle profile plots of 2000 data showing the strength of attenuation and subsurface geologic features. 50 MHz data (a) is plotted to a maximum depth of 13 m, 100 MHz (b) to a maximum depth of 9 m and the 200 MHz (c) to a maximum depth of 6.1 m. Traces are sampled at 0.125 m. Lake elevation at the time of data collection is 159.57 m. The uppermost thin yellow line in each figure is the free surface topography. Plotted depths are relative to the highest elevation on the line, at ~12 m, not relative to the topography.....42

Figure 23. (a) 50MHz, (b) 100 MHz and (c) 200 MHz matrix and wiggle profile plots of 2002 data showing the strength of attenuation and subsurface geologic features. 50 MHz data (a) is plotted to a maximum depth of 13 m, 100 MHz (b) to a maximum depth of 9 m and the 200 MHz (c) to a maximum depth of 6.1 m. Traces are sampled at 0.125 m. Lake elevation at the time of data collection is 162.2 m. The uppermost thin yellow line in each figure is the free surface topography. Plotted depths are relative to the highest elevation on the line, at ~12 m, not relative to the topography.....43

## LIST OF TABLES

Table 1. Lake elevation readings and their respective dates of GPR data collection acquired from the Fort Worth Army Corps of Engineers, 2017. GPVT2 ELEV. OBS. FT-NGVD, all readings are converted from feet to meters.....	11
--	----

# **CHAPTER 1**

## **INTRODUCTION**

The electromagnetic properties of rocks are related to their composition and water content, both of which control the speed of Ground Penetrating Radar (GPR) wave propagation and their attenuation (e.g., Xu and McMechan, 1997). The contrasts in relative dielectric constant and conductivity between adjacent rock layers give rise to reflection of incident electromagnetic waves (Reynolds, 2011; Grunewald, 2017). The shape of the capillary transition zone (CTZ) depends on the pore-size distribution of the soil and has a strong influence on the signature of the GPR reflections (Igel et al., 2016). The depth of the onset of signal attenuation gives an indication of the position of the water table (Taherian et al., 1990) in each of the 8 survey years. Known lake levels obtained from the Fort Worth Army Corps of Engineers records (GPVT2 ELEV., 2017) at Grapevine Lake, Texas, provide accurate relative positions of the local water table in the Woodbine Formation at the time of each survey.

This research is facilitated by the availability of previous GPR data containing visible differences as a function of water table position over time. Studies of GPR detection of the water table include Kowalczyk et al. (2018), Klotzsche et al. (2018), Seger and Nashait (2011), Doolittle et al. (2005) and Bentley and Trenholm (2002). Kowalczyk et al (2018), showed water table changes using GPR data collected five times within 1 year. They compared their results with piezometer data and concluded that GPR can detect the water table with standard error of 0.088. Seger and Nashait (2011) compared underground water determination by drilling, to the results of GPR data and concluded that GPR is an effective method for detection of underground water level. Bentley and Trenholm (2002) reveal that the main sources of depth uncertainty are errors in the

GPR velocity estimates and in predicting the thickness of the capillary fringe. Bentley and Trenholm's work also shows that, under favorable circumstances, and using 200 MHz GPR data, the elevation of shallow water tables can be estimated with an accuracy on the order of 0.2 m. Klotzsche et al (2018) and Doolittle et al. (2005) have shown that over a 2 to 3-year period, GPR can effectively reveal systematic temporal and spatial variations in water table depths and local groundwater flow patterns. An important parameter in analysis is the velocity with which the radar signals travel through the different rock strata recorded with their respective two-way travel times (e.g., Parsekian, 2018; Cai and McMechan, 1995).

Precipitation increases the spatial variability of rock water content (Grote et al., 2010). Explicitly including the free surface topography into Kirchhoff migration and the results of velocity analysis aids the computation of the depth of the water table along the survey line (Doolittle et al., 2005). Determination of the depth to the water table can be used to define the availability of ground water in areas where water is needed. GPR can also potentially be applied to flood-prone areas to determine the volume of water that would raise the water table to the surface and thereby cause flooding in periods of heavy rainfall.

## **1.1 Geology of study area**

The Woodbine Formation outcrop at the project site is primarily fine to medium grained sandstone and is a hydrocarbon producing formation in the East Texas oil field. The Woodbine contains ancient river and delta systems that originated from weathering and erosion of the Ouachita uplift in Oklahoma and Arkansas and the Sabine uplift in Texas and Louisiana (Bunge, 2007). Its deposits are primarily terrigenous near shore and shallow marine depositional systems and include fluvial, deltaic and shelf deposits (Oliver, 1971; Main, 2006). The Woodbine

Formation is Late Cretaceous (Hundnall and Eaton, 1968) and belongs to the Gulf Series (Dodge, 1969). It contains 175 to 250 feet of sandstones and shales (Oliver, 1971).

The structure of the Woodbine exposed in Dallas-Fort Worth area is homoclinal, with average strike approximately N30°E (Lee, 1997). The Cretaceous rocks have undergone little deformation since the time they were formed. Vertical fractures are found locally in the layers of Woodbine sandstone which are interbedded with clay. There is southward thinning of the Woodbine because of interfingering with the Eagle Ford Formation (Dodge, 1969).

The Woodbine is the basal stratigraphic unit of the Upper Cretaceous. It unconformably overlies marine shale and limestone of the Grayson Formation, and is overlain unconformably by marine shales of the Eagle Ford Group (Scheihing & Lorsong, 1995). The four rock members of the Woodbine in ascending order are the Rush Creek, Dexter, Lewisville and Arlington members (Figure 1).

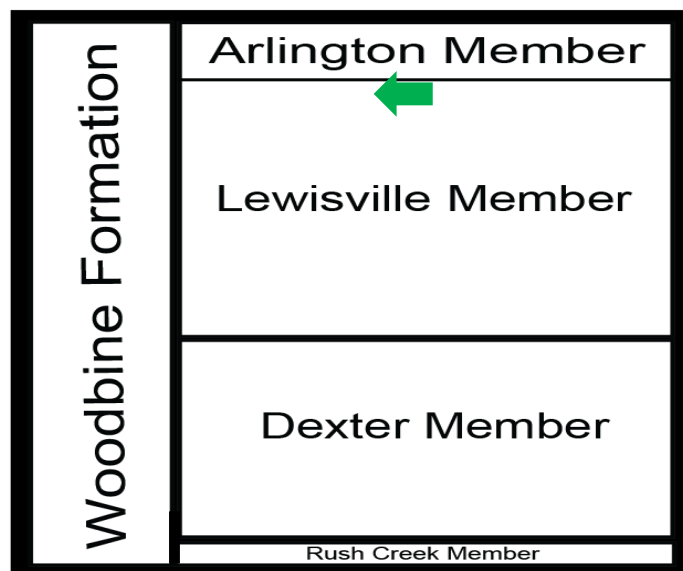


Figure 1. Stratigraphy of the Woodbine Formation. The green arrow shows study location. Modified after Bergquist (1949) and Dodge (1969).

At the study location, the upper part of the Lewisville Member of the Woodbine Formation, outcrops. It has reddish-brown to grey colored sandstone that contains ironstone cement and concretions (Dodge, 1969) which is fairly laterally continuous in the upper part of Unit 7; also there are numerous permeability zone fractures with varying amount of hematite infill (e.g., ~23 m position) with appreciable permeability of  $\sim >1$  that allows water to travel through it.

A distinctive conglomeratic lag at the base of the ironstone beds which cuts through interbedded thin sandstones and clay containing carbonaceous plant fragments and marine fossils identifies the Lewisville Member (Bunge, 2007). Generally, the upper portion of the Lewisville Unit is more arenaceous than the lower and there are large selenite crystals which are locally embedded in the shale (Scheihing & Lorscheid, 1995). The ferruginous conglomerate caps the exposed section and forms an excellent example of a transgressive lag and, together with its thickness, represents a significant unconformity between the Lewisville Member below and the Eagle Ford Shale above.

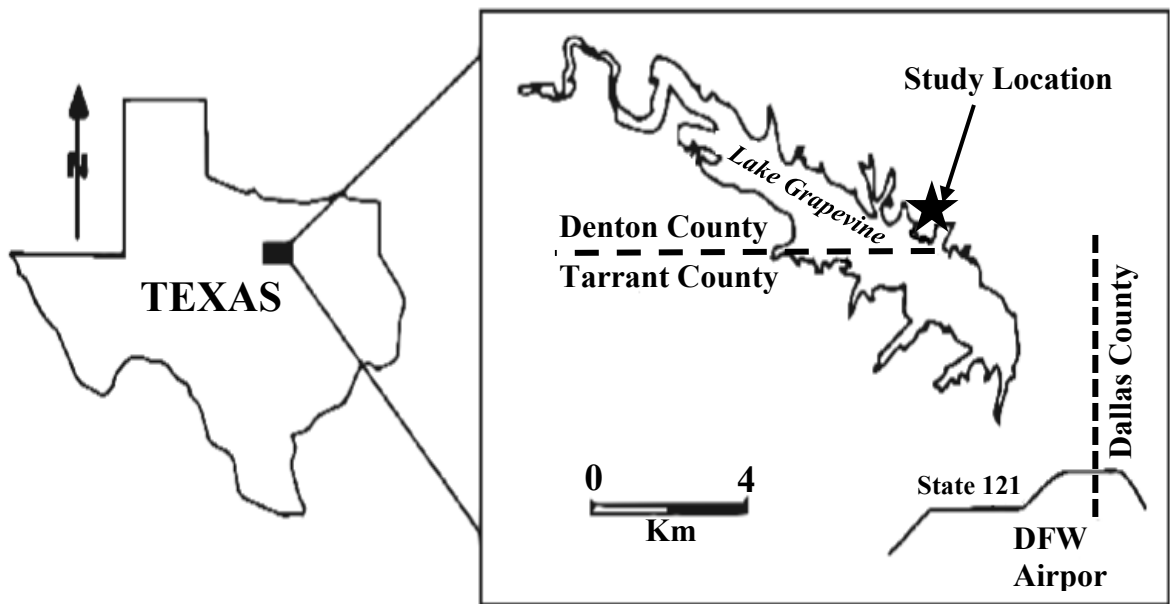


Figure 2. Map showing the study location along the north side of Grapevine Lake. Modified after Lee, 1997.





Figure 3. Location of GPR survey line along Grapevine Lake. Modified from Google Earth 2017.

Many of the sandstone beds show rippled surfaces and cross-laminated structure (Lee, 1997). Main (2006) interpreted the Lake Grapevine delta sequence as being a fluvial influenced system because of the amount of sand observed in the delta front and delta plain environments. Outcrops form small bluffs at the lake shore immediately west of the parking lot at Fishing Trail No. 2 in Murrell Park on the north shore of Lake Grapevine, Denton County, Texas (Figure 2). Several meters of heavily oxidized, ferruginous fluvial sands overlying a sandy clay base constitute the lithology of this section (Figure 3). The sands are lenticular, bedded and are interpreted as fluvial channel sequences which coarsen upwards (Main, 2006).

The upper 5.07 m of the outcrop contain the following lithologies in order from the top to bottom of the cliff face (Scheihing & Lorsong, 1995).

**Unit 7 (0 m-1.6 m):** Pebbly conglomerate with ironstone-cemented concretions at the top (Figure 4). It contains thick layers of sandstone that alternate with mudstone. It is covered by a light layer of freshly eroded loose sand that is rich in iron.

**Unit 6 (1.6 m-1.94 m):** The contact of this unit with Unit 7 is gradational. Unit 6 consists of fine-grained, moderately well sorted, burrowed and rippled sandstone with desiccation cracks (Figure 5). The bottom part of this unit contains a few centimeters of clay.

**Unit 5 (1.94 m-2.195 m):** The contact of this unit with Unit 6 is gradational. Unit 5 consists of trough cross-stratified mudstone grading upward into ripples at the top (Figure 5).

**Unit 4 (2.195 m-2.54 m):** The contact of this unit with Unit 5 is gradational. Unit 4 consists of rippled sandstone (Figure 5).

**Unit 3 (2.54 m-3.9 m):** The contact of this unit with unit 4 is gradational. Unit 3 consists of fine-grained, moderately well sorted, sandstone with small scale trough cross-stratification (in sets less than 10 cm) and straight crested ripples at the top (Figure 6).

**Unit 2 (3.9 m-4.48 m):** The contact of this unit with unit 3 is gradational. Unit 2 consists of ripple laminated, flaggy bedded, orange to ochre fine-grained, well sorted sandstone with possible wave ripples on exposed surfaces and interbedded with flagged clay at the base.



Figure 4. Red ironstone-cemented pebbly conglomerate with concretions at the top of Unit 7.

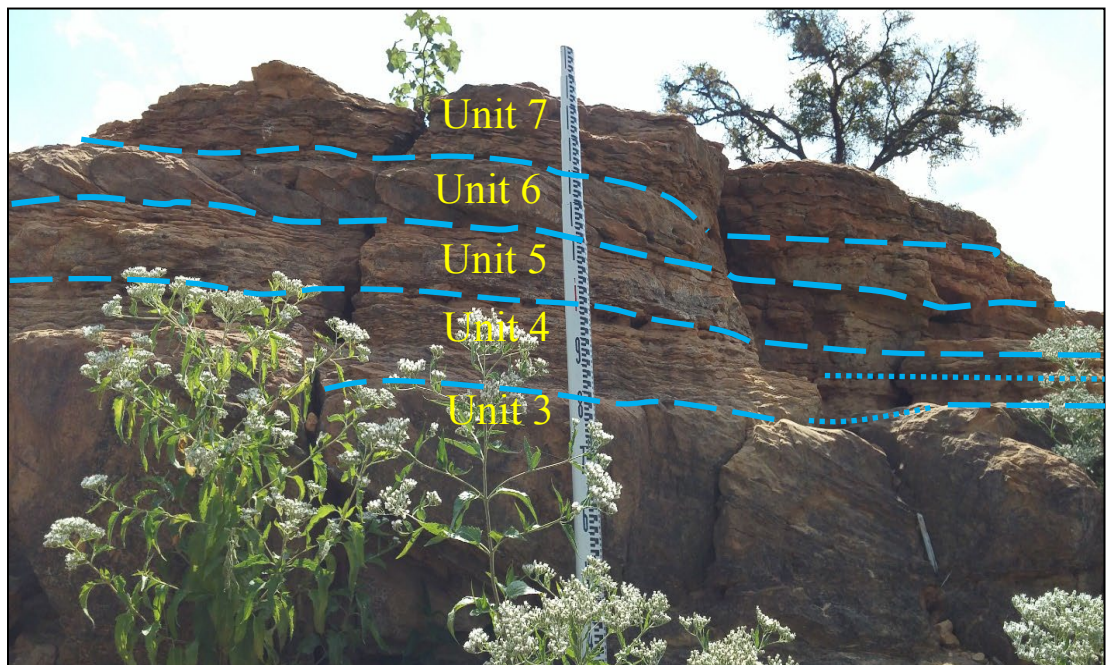


Figure 5. Exposed cliff face section showing lithologic units. Tidal channel sandstones grading upwards into rippled flaggy bedded tidal flat sandstones at Fishing Trail 2, Murrell Park.



**Unit 1 (4.38 m-5.07 m):** This unit consists of very fine-grained sandstone more than 1.74 m thick and coarsens to fine-grained sandstone to the top. It is trough cross-stratified, with straight crested ripples and burrows on foresets as well as clay clasts on scour surfaces. Trough cross sets are between 15 cm and 30 cm thick.

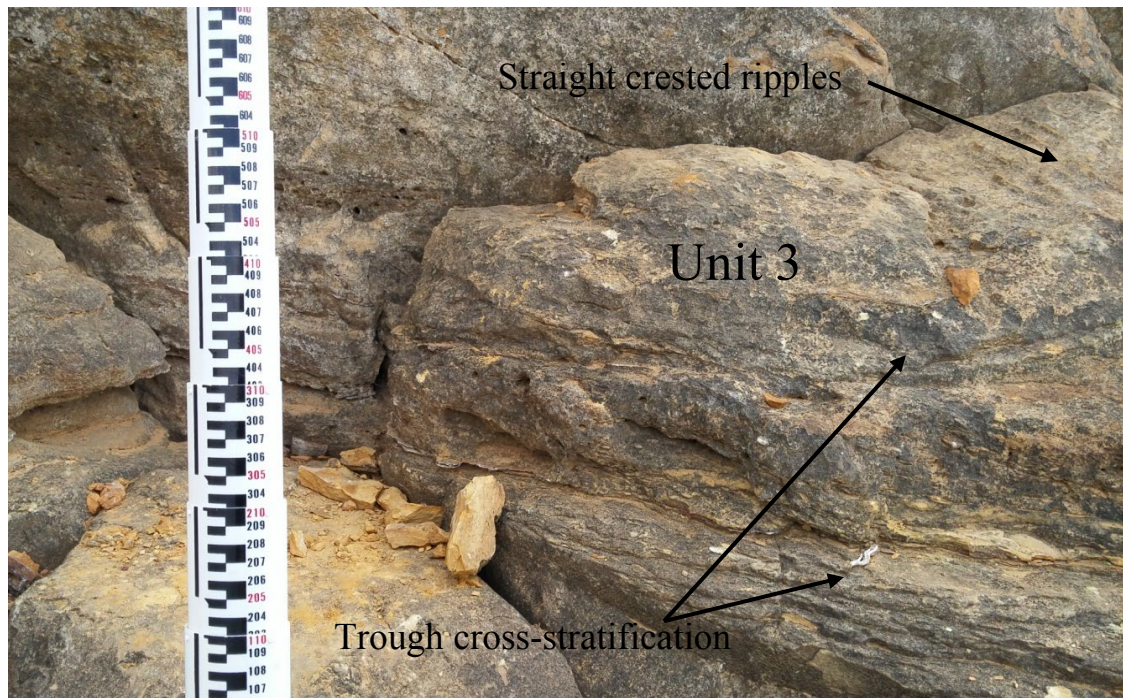


Figure 6. Lithologic Unit 3. Fine grained moderately well-sorted sandstone showing small scale trough cross-stratification and straight crested ripples at the top.

## **CHAPTER 2**

### **RESEARCH METHODOLOGY**

#### **2.1 GPR METHOD**

GPR is a near surface geophysical technique that makes use of electromagnetic waves to construct 2D or 3D images of the subsurface (e.g., Davis and Annan, 1989). It works by producing a short pulse of high frequency (10 to 1000 MHz) electromagnetic energy which is directed into the shallow subsurface (Bentley and Trenholm, 2002). These waves are reflected, refracted and attenuated depending on the electromagnetic properties of the subsurface. Rocks are quite variable in their electrical properties with conductivities ranging from  $10^4$  to  $10^{-14}$  S/m (Gueguen and Palciauskas, 1994). Rocks at the survey site are sandstone and are expected to have conductivities ranging from  $10^{-3}$  to  $10^{-5}$  S/m.

Sandstone materials at depths below the water table are saturated and may have conductivity values up to  $10^{-2}$  S/m (Reynolds, 2011). Such a large range implies that electromagnetic methods can be powerful tools in the detection of areas of anomalous conductivity associated with rock water content. There is an increasing loss of electrical energy from radar signals as they travel through rocks which are electrically conductive (Taherian, 1990). Propagation of electromagnetic radiation is described by Maxwell's equations (e.g., Annan, 2005). GPR has been used for geological applications since the 1960s, when it was first used in connection with the development of radio echo-sounding of polar ice sheets (Bradford, 2007). Subsequently, advanced data processing software has made GPR a very important geophysical

tool for high resolution studies of the shallow subsurface (e.g., Fisher et al., 1992b). GPR has been used to investigate the movement and behavior of the water table (Davis and Annan, 1989).

## **2.2 Research Objectives**

Eight GPR profiles and Common Mid-Point gather data sets were collected on the same line, every two or three years from 1998 to 2017. This research is unique because the GPR data span about 2 decades; at the times of the surveys, the lake water level varied from 159.57 m to 162.97 m (Table 1). Changes in the attenuation and velocity of GPR signals can be obtained from these data sets and compared and analyzed as a function of the known position of the lake level. The presence of iron oxide in the top layer strongly attenuates the GPR waves. Therefore, the objectives of this research include:

1. Mapping and measuring geologic features present in a cliff face exposure that lies parallel to the survey line.
2. Analyzing and interpreting 2D radar profiles in terms of GPR velocity and attenuation.
3. Estimating the depths to the water table in each of the survey years from the GPR data and how they relate to the known water level of the lake at those times.
4. Investigating the effect of the presence of hematite, in the top layer on the strength of the GPR signal.
5. Analyzing GPR data as a function of fresh and ground water distribution and estimation of fresh water quantity using calculations from the porosity of the Woodbine aquifer and for the characterization of the reservoir analog.

### 2.3 Data acquisition and field work

The pulseEKKO GPR 100 system used for this study consists of four main elements; the transmitting unit, the receiving unit, the control unit and the display unit (Figure 7). The transmitter produces a short duration, 1000-volt pulse, which is applied to the transmitting antenna that radiates the pulse into the ground. This transmitted signal travels in the ground and is reflected, by

Table 1. Lake elevation readings and their respective dates of GPR data collection acquired from the Fort Worth Army Corps of Engineers, 2017. GPVT2 ELEV. OBS. FT-NGVD, all readings are converted from feet to meters.

Date of Data collection	Lake Elevation (m)
September 26 <sup>th</sup> , 1998	161.7
September 30 <sup>th</sup> , 2000	159.57
September 28 <sup>th</sup> , 2002	162.2
September 24 <sup>th</sup> , 2005	161.8
October 4 <sup>th</sup> , 2008	161.5
October 8 <sup>th</sup> , 2011	161.7
September 27 <sup>th</sup> , 2014	159.59
September 23 <sup>rd</sup> , 2017	162.97

the various contrasts in dielectric permittivity and electrical conductivity, back to the receiving antenna, and then to the receiver. The receiver amplifies the signals and formats them for display by the control unit and are finally saved on the hard disk of the computer (Sensors and Software<sup>®</sup>, 1996). Within any geologic section, GPR is able to map the water table as well as the capillary fringe, associated with changes in the dielectric constant and the electrical conductivity of the subsurface (Kowalsky et al., 2005).

Surveys were performed at 2-year or 3-year intervals at the same location using a 1000 v transmitter and receiver combination in the years 1998, 2000, 2002, 2005, 2008, 2011, 2014 and 2017. For all surveys, GPR data were acquired along a 50 m measuring tape stretched along the ground from the north to south near the cliff face (Figure 8). The measuring tape serves as the reference line along which GPR signals are recorded (Liu, 2006). Data collected include common mid-point gathers and profiles at 50 MHz, 100 MHz and 200 MHz frequencies, elevation data to be used for topographic corrections and photos of the location and rock outcrops, as well as hand samples of each stratigraphic unit. The transmitter-to-receiver offset for the common-offset

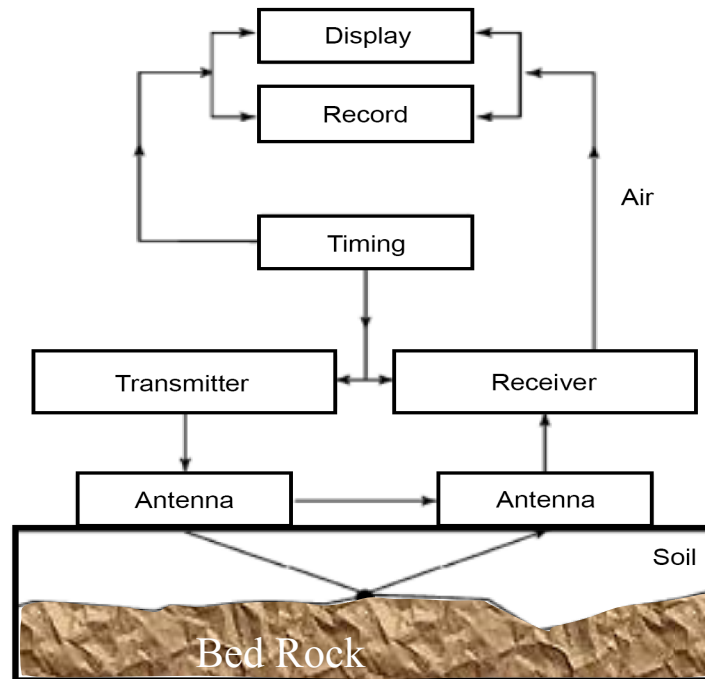


Figure 7. Block diagram depicting main components of a ground penetrating radar system (Modified after Sambhaji, 2016).

profiles is fixed at 2 m and the trace spacing was 0.5 m. A 256-trace stack was recorded and saved at each receiver location along each profile. Common Mid-Point data were collected at a 0.25 m constant half-offset increment for a total of 149 traces.





Figure 8. Sensors & Software® 100 MHz transmitter and receiver ready for data collection.

a)



b)



Figure 9. (a) Rod and (b) tripod-mounted level and for measuring water level and topography.

The mid-point gather was centered (Figure 8) at the 25 m mark on the tape; this serves as the primary data in determining the velocity profile, and hence depth to the water table, at that position. A rod and the tripod-mounted level combination (Figures 9a and 9b) are used to measure the lake water depth below the midpoint. They are also used to measure the relative topography of each point along the survey line (Figure 10), which is required input for doing the subsequent Kirchhoff migration; the topography is used as the datum for implicit correction of elevation statics (Figure 11).

## 2.4 Data processing and analysis

The acquired CMP data were first processed for velocity analysis which is required for profile plotting and migration. For analysis of the amplitudes of the profile data, each profile is plotted with a calibrated gain. Lake elevation data obtained from the 24-hour records of the Fort



Figure 10. Tape measure on the ground showing the 50 m long survey line.

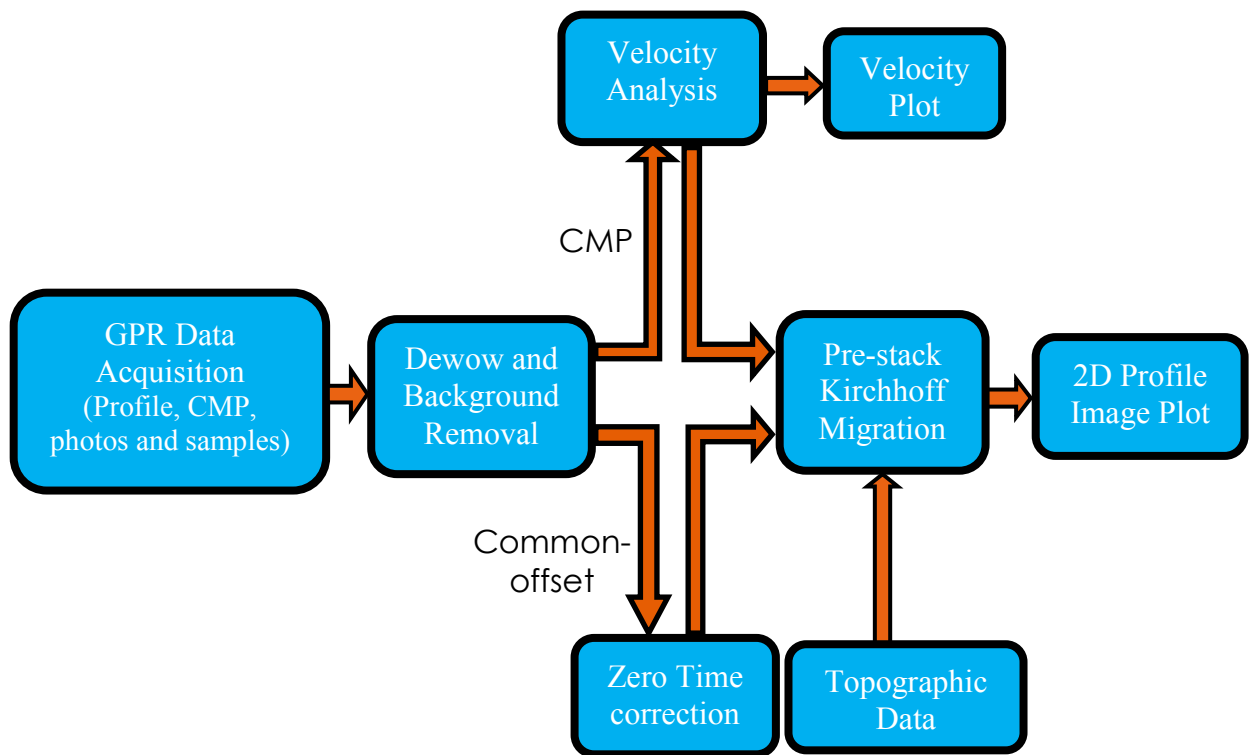


Figure 11. Flow chart for GPR Data collection, filtering/processing and analysis. Modified after Fisher et al., 1992a.

Worth Army Corps of Engineers (GPVT2 ELEV., 2017) show the lake level at each survey time as well as the rising and falling water levels between the surveys (Table 1). This study includes comparing the effect of the changing water level of the lake on the water table position and studying amount of attenuation caused by additional fresh water from rainfall, in the GPR data in each of the years when the data were collected.

Although data from all the years is processed and analyzed, more time is spent to analyze data from survey years 2017, 2014, 2011, 2008 and 2005 which contain data when the water level was highest, intermediate and the close to the lowest value (Figure 12). These data have been strategically selected for examination because we expect to see the largest differences in radar



amplitude and velocity when subsurface rocks are fully saturated versus when they are least saturated with water.

#### 2.4.1 GPR data processing

Various filters are applied to raw GPR field data to improve the data quality by removing different types of noise which can be of very high or very low frequency. Basic GPR processing includes dewowing and time zero corrections. Dewowing fits and subtracts the exponential background signal of the capacitive decay between the antenna and the ground surface to emphasize the dominant frequency band around the spectral peak of the transmitted signal (Sambhaji, 2016). Time zero corrections align all the first arriving (air) waves to the same time to

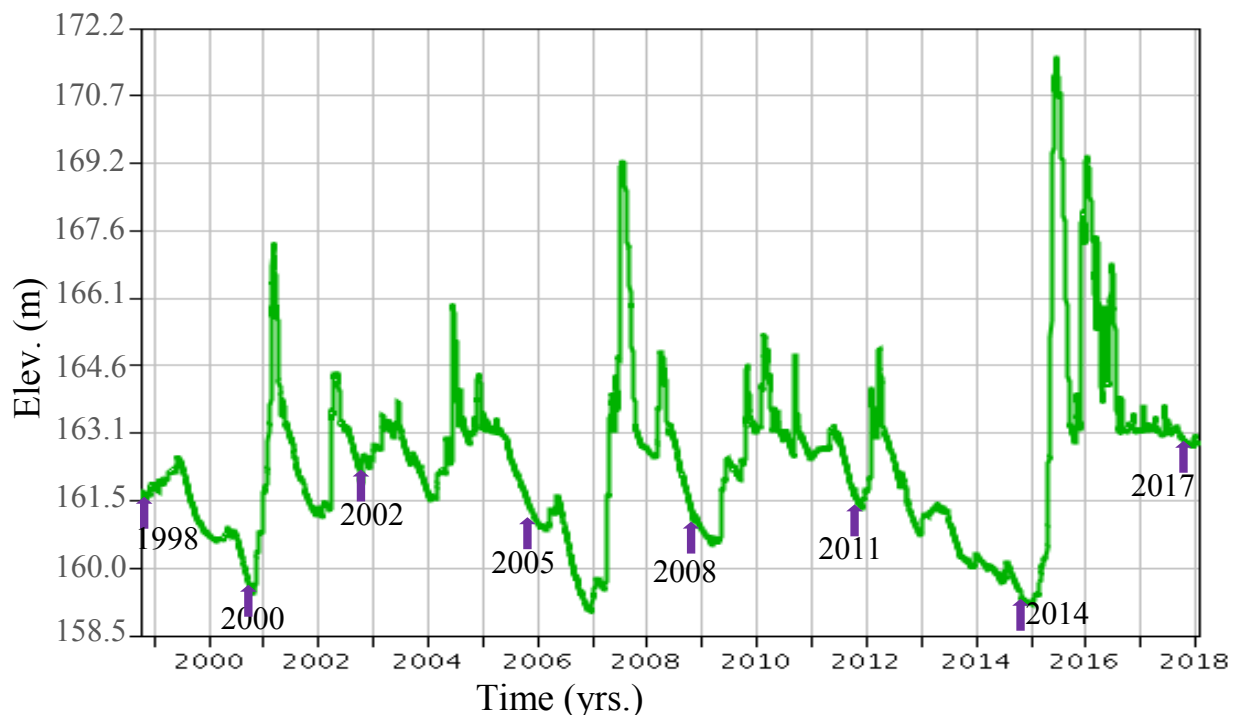


Figure 12. Plot of lake elevations against data acquisition years. Modified after Fort Worth Army Corps of Engineers, 2017.

correct for both local time shifts and long period drifts. Trace differencing replaces each trace by the difference between itself and the previous trace (Sensors and Software<sup>®</sup>, 1996) which acts as a dip filter that removes all constant-time features, such as the time-zero-corrected air waves, flat reflections in profiles, and stacking artifacts in RMS velocity scans (Figure 13).

#### **2.4.2 Velocity analysis**

Velocity analysis can be performed by sweeping through a range of RMS velocities, applying the calculated moveout correction for each zero-offset time in the CMP, and stacking the corrected data at constant time to determine the RMS velocity that flattens the moveout corrected data. The importance of velocity analysis in radar data processing is the extraction of RMS velocity versus depth functions from the sounding data (Xu and McMechan, 1997). Procedures for reliable picking of velocity events are detailed by Harbi and McMechan (2011).

The PulseEKKO<sup>®</sup> software enables an RMS velocity calculation from the CMP data and plotting the result for interpretation. The velocity is necessary to determine the depths to targets. The offset increment from trace-to-trace, centered on the CMP mark, is required for accurate calculations (Cassidy, 2008). The velocity trajectory in the RMS velocity versus two-way time is determined by following the largest amplitude through time (Lee et al., 2005).

2017 and 2000 are the two years when the water level of the lake reached the maximum and minimum values, at the time of the respective surveys. For the minimum, we prefer the 2014 data rather than 2000 because the former contains less noise. The difference in the water levels between 2017 and 2014 is 3.38 m (Table 1). For the maximum difference in electric and dielectric

attributes, in terms of attenuation caused by rock saturation (Figure 13), it is appropriate to examine the effects of the water level on the GPR velocities and attenuation of these two years.

### **2.4.3 Comparing velocity models at different lake levels**

The velocity of light in air is  $\sim 0.3$  m/ns (Reynolds, 2011). The RMS velocities and their travel times need to be picked for accurate interval velocity analysis. Figure 14 shows the 50 MHz interval velocity versus depth functions from 2017, 2014, 2011 and 2008. Each of data were collected at different times when the water levels were different (Table 1). GPR signals in the 50 MHz CMP profiles are attenuated at two-way reflection times greater than  $\sim 160$  ns, which are times equivalent to  $\sim 6$  m depth (Figures 13 and 14). Beyond this depth, no clear record of velocity is available. As the water level rises, the velocity curves shift to lower interval velocity values (Figure 14).

GPR velocities of years with the largest water level difference correspond to the largest difference in water saturation, and hence, attenuation. Velocity models from the four CMP data all follow and have similar shapes (Figure 14). The velocities in all the four curves drop to their lowest values (0.052-0.065 m/ns) near 1.7 m depth, suggesting water saturation in high porosity. GPR velocity is determined by the water saturation and the signal attenuation is determined by the electrical conductivity of the water (Sensors and Software<sup>®</sup>, 1996). A drop in GPR velocity and signal amplitude versus depth is associated with water saturation and the conductivity respectively; the latter is controlled by its salinity or total dissolved solids (Nabighian, 1988).

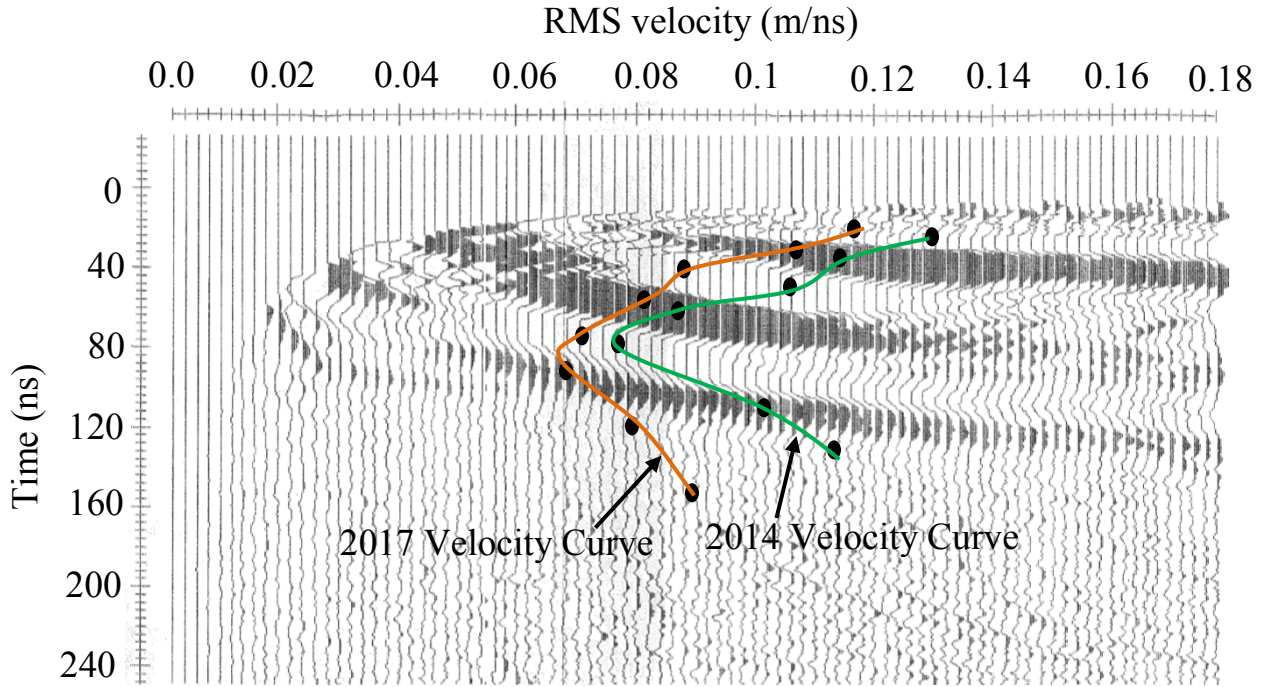


Figure 13. Plot of 2017 and 2014 50 MHz RMS velocity curves superimposed on the 2014 time data. 2014 (the green curve) has velocities ranging from 0.13 m/ns to 0.76 m/ns corresponding to the low water content. 2017 (the orange curve) has the highest recorded water level with highly saturated rocks slowing down GPR velocities to ranges from 0.116 m/ns to 0.68 m/ns.

#### 2.4.4 2D Pre-stack Kirchhoff Migration

Profile data of 2017 and 2014 are plotted in Figure 15 after the pre-processing is complete. At this stage, no migration or topographic correction is applied; these show the data character that is input into migration.

##### 2.4.4.1 2D velocity grid

The input velocities for migration are defined at equally spaced grid intervals that may have equal or unequal dimensions (McMechan and Epili, 1992). The 2D velocity grid increments used for migration of the GPR profile data in this analysis are  $0.125 \times 0.125$  m. The grid

dimensions are  $(x, z) = (473, 105)$  points for the 50 MHz profiles,  $(x, z) = (473, 75)$  for the 100 MHz profiles and  $(x, z) = (473, 50)$  for the 200 MHz profiles. We add 24 extra voxels at the north and south ends to retain reflections that dip toward the grid edges.

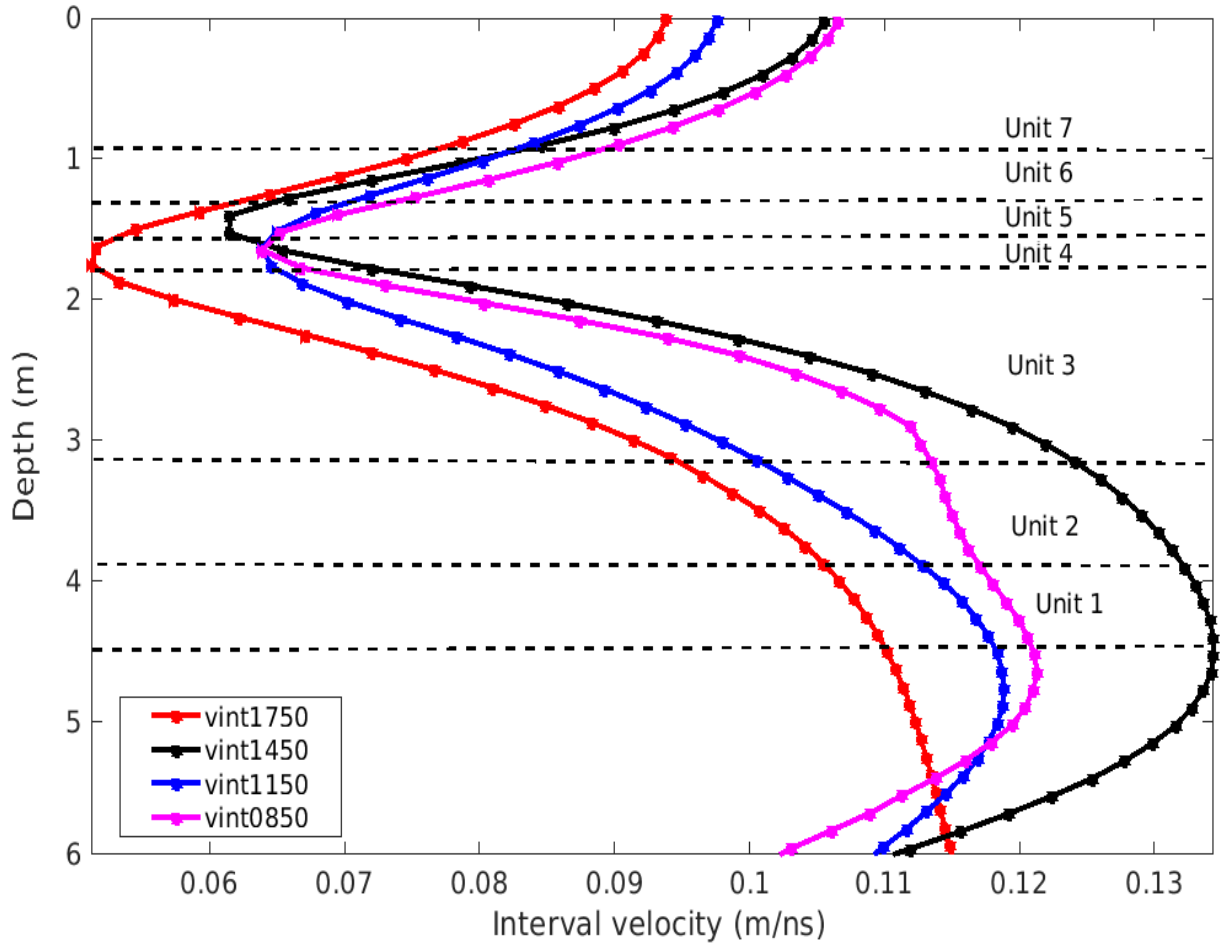


Figure 14. Interval velocity-depth plot showing the 50 MHz velocity curves of 2017, 2014, 2011 and 2008 superimposed on the lithologic units. The 2014 data (black curve) shows maximum velocity while 2017 (red curve) has the least velocity at most depths. 2011 and 2008 (blue and pink curves) have intermediate velocities with values that lie between those of 2014 and 2017.



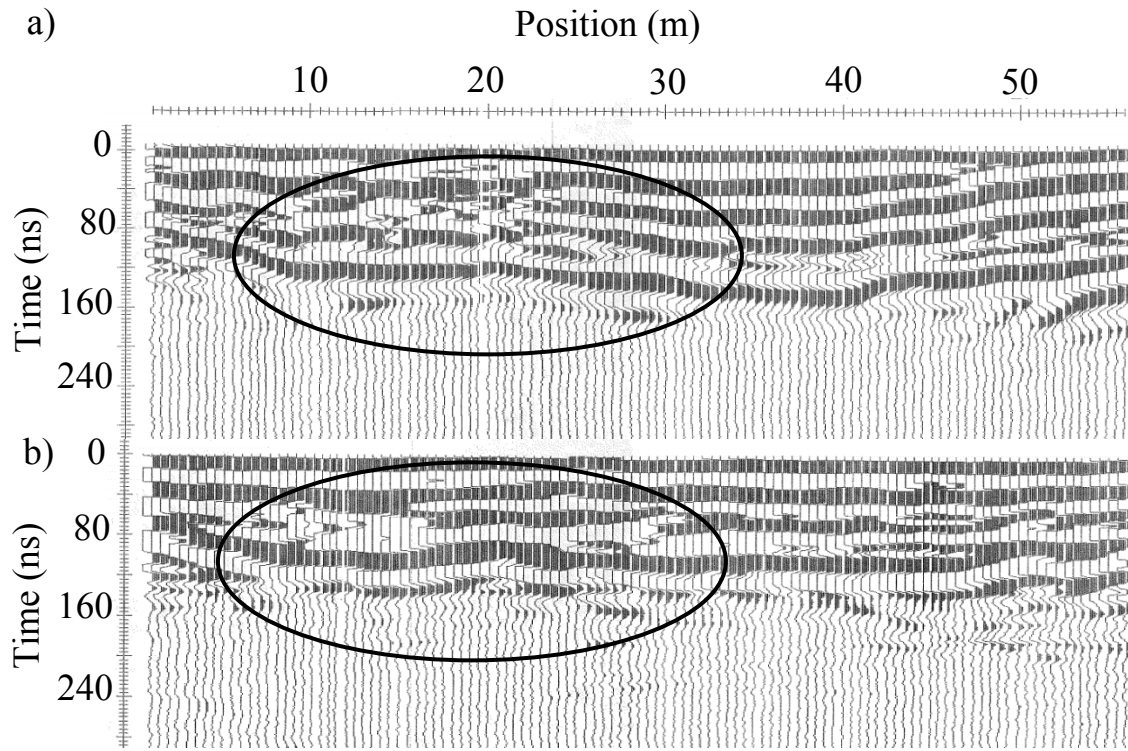


Figure 15. (a) 2017 and (b) 2014 50 MHz profiles after dewowing and time alignment. Oval circles enclose less coherent areas at the left-hand side of each profile. See interpretation section below.

#### 2.4.4.2 2D ray tracing and two-way time map construction

Rays are traced from each survey (transmitter or receiver) point to each grid point on the chosen image plane to calculate the image times. The output is a 2-D grid of time indexes of the one-way travel times (McMechan and Epili, 1996). For a given transmitter and receiver pair (i.e., one GPR trace), two-way times are obtained for each grid point, by summing the two corresponding one-way time maps for the transmitter and receiver locations.

#### 2.4.4.3 Migration

The final step in the migration of a single time sample is to insert its amplitude into the image plane at all the grid points that have the corresponding two-way time (McMechan & Epili,

1996). The final image for a profile of traces is obtained by summing the imaged amplitude contributions of all traces, over all image times at each image point. It takes an unfocused (distorted) finite-offset time section and produces a migrated, focused, depth section. Elevation variations are included by using the topography as the datum (Figure 16). The resulting migrated 2D images are plotted by superimposing the output amplitudes in two formats, wiggle traces and color scale. This improves clarity and reduces uncertainty in depth determination and identification of subsurface lithologic layers (Figure 16).

## CHAPTER 3

### RESULTS AND INTERPRETATION

#### 3.1 Subsurface geological features.

Comparing the pre-migration GPR data in Figure 15 (a and b) to their corresponding post-migration data in Figure 16 (a) and (b) shows the input image quality associated with the migration. For example, the rock layers that tend to follow the topography in Figure 15(a) are

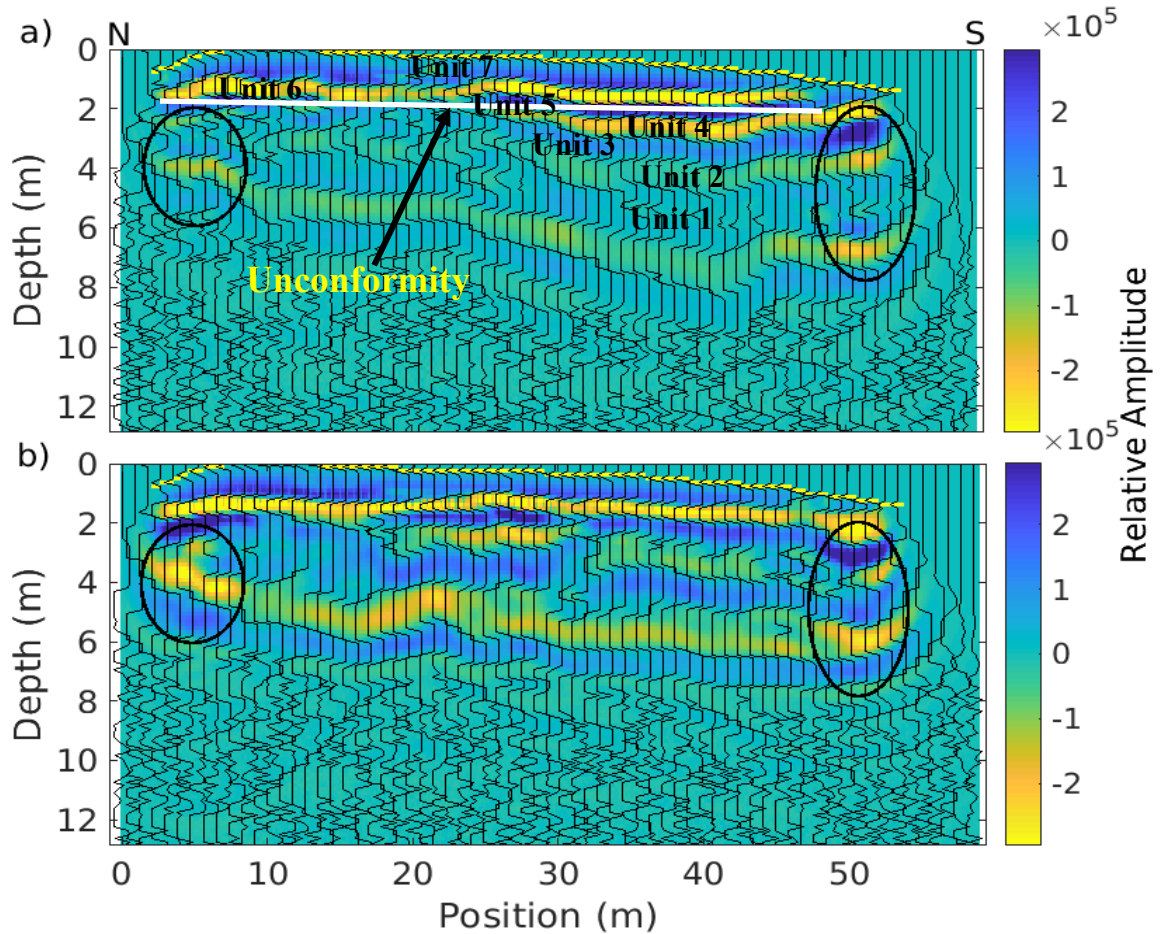


Figure 16. (a) 2017 and (b) 2014 50 MHz profiles after application of Kirchhoff migration using the measured topography as the datum. The uppermost thin yellow line is the free surface topography.

moved to their correct relative positions in Figure 16(a) and reveal their true elevations. The color-differentiated amplitudes with wiggles plots used in the post-migrated profiles of Figures 16 (a) and (b) make it easier to visually detect changes in GPR amplitudes.

The adsorbed water in the clay layers which occur as interbeddings within units 6, 5 and 4 is the probable cause of the drop in GPR velocities at  $\sim 1.7$  m depth (Figure 14). Saturated clay layers have velocities as low as 0.047 m/ns to 0.09 m/ns and high conductivities of between 20-1000 mS/m (Reynolds, 2011); this is consistent with our data. Also, the high relative velocities near 4.4 m depth (in Figure 14) suggest that units 2 and 1 have lower porosities than the shallower units. The locations of the perturbations of the rate of velocity changes at  $\sim 1.7$  m,  $\sim 3.2$ ,  $\sim 3.7$  m and  $\sim 4.8$  m depths indicate the locations of boundaries between the layers, which have different water content, mineral composition and rock physical properties. The right-hand side of both profiles in Figure 15 (a) and (b) is more coherent, implying that the rock layers are more continuous.

The north end of the profile is incoherent with features such as joints and faults dominating areas in the ovals between positions 6 m and 30 m. These are more visible in the pre-migration profiles of Figure 15, than in their post-migration versions of Figure 16, because the GPR data are 3D but are processed as 2D; thus, some out-of-plane discontinuities are smeared and are less visible after migration. The rapid attenuation of radar signals in depth implies the existence of a capillary fringe which gradually increases to full saturation at the water table.

The south-end of the 50 MHz 2D images reveal  $\sim 9$  distinct rock layers of the subsurface that are identified from 0 m to  $\sim 9$  m depth in 2017 and to  $\sim 7.8$  m depth in 2014 (Figure 16a). Of

these, only the upper 7 layers appear above the lake water level through the years of this survey and have been identified as lithologic units in Figure 16(a). These units are predominantly fine-grained sandstone with clay interbedding. The behavior of these strata and their features are well established in these models. For example, the strata at depths less than the unconformity at 2 m (units 7, 6 and 5) are relatively flat. The underlying stratigraphy contains a local top truncated syncline with apparent dips on its flanks of  $<6^\circ$ .

### **3.2 Analysis of 2D GPR data with respect to the water table position.**

The ability of GPR to detect the water table is a direct consequence of the contrast between the electric and dielectric properties in the transition from unsaturated to saturated rock. The water table is generally flat, as its position is primarily determined by gravity, and thus cuts across dipping lithologic boundaries (e.g. Fisher et al., 1992a). The water table is locally perturbed by variable capillary effects associated with changes in grain size and pore structure. Compare Figure 16a, in which a strong water table reflection hides the lithology, with Figure 16b, in which it does not. The GPR data recorded at any time contains the superimposed signatures of both the time-independent sedimentology and the time-dependent distribution of the water. The GPR velocities and attenuations are both affected by the water distribution and chemistry.

Identifying the effects of different positions of the water table requires GPR data collected at the corresponding times. Figure 17 shows the 50 MHz, 100 MHz and 200 MHz profiles each for the survey years 2014, 2005 and 2017. The water level for 2017 is highest ( $\sim 162.97$  m), that of 2005 is intermediate ( $\sim 161.8$  m) with 2014 recording a lower water level ( $\sim 159.59$  m) (Table 1).

For a realistic comparison and analysis, equal amplitude scaling and depth extents are maintained when plotting data of the same frequencies.

The strength of GPR attenuation and the depth of penetration are dependent on the frequency used for the data collection; hence the 50 MHz, 100 MHz and 200 MHz data are plotted to depths ~13 m, 9 m and 6 m respectively (Figures 17(a), 17(d) and 17(g)). At any given depth in 2014, when the water level is lowest among the three chosen data sets, larger amplitudes are seen at the same depth because of the low water content of the rocks above the water table (Figure 17(a)). This is not the case in 2005 when the water table was 2.21 m closer to the surface, saturating the overlying rocks and therefore producing lower amplitudes at the same depth and position (Figure 17(b)).

At depths less than ~1.8 m, the 50 MHz and 100 MHz GPR profile data of both 2014 and 2005 show the same amplitudes. This is because rocks at this depth in both datasets are ~equally unsaturated with less conductivity, and thus facilitates radar penetration. Again, attenuation in the 2014 50 MHz data (Figure 17(a)) is low and starts at depth ~5.8 m at the north end to as deep as 7.6 m at the south end compared to the corresponding 50 MHz data of 2005 (Figure 17(b)) in which attenuation starts at smaller depths of ~3 m at the north and ~5 m at the south end. This is better revealed in the (higher resolution) 100 MHz data [Figures 17(d and e)].

The 100 MHz data also confirms the influence of the water level on the water table, as larger amplitudes are recorded in 2014 down to depths of ~5 to 7 m, while the amplitude at the same depths in 2005 are comparatively very low because of the shallower water table. In the 100

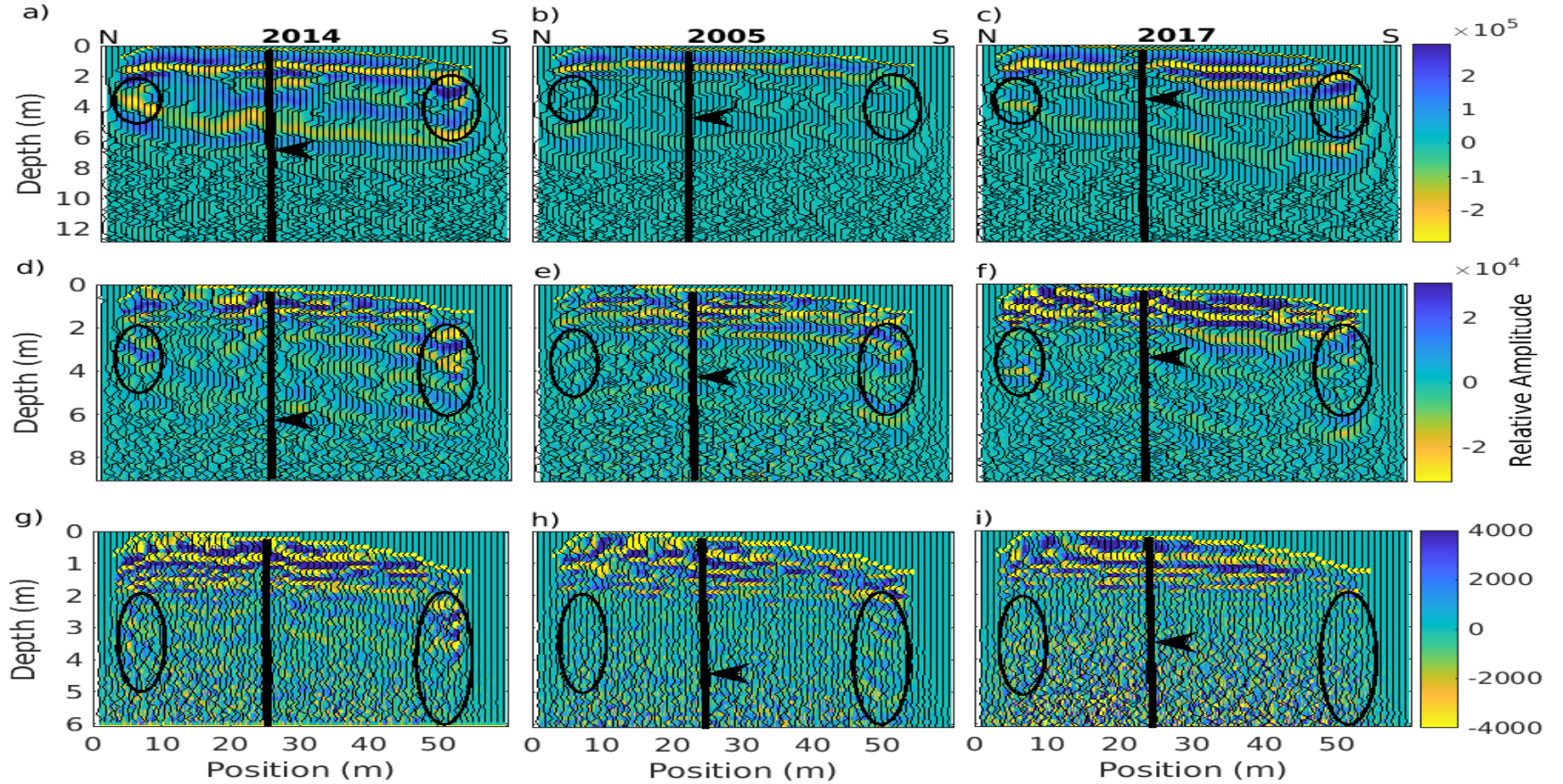


Figure 17. 50 MHz, 100 MHz and 200 MHz matrix and wiggle profile plots of 2014 (a, d and g), 2005 (b, e and h) and 2017 (c, f and i) data showing the water table, level of attenuation and subsurface geologic features. All 50 MHz data (a), (b) and (c) are plotted to a maximum depth of 13 m, 100 MHz to a maximum depth of 9 m and the 200 MHz to a maximum depth of 6.1 m. Traces are sampled at 0.125 m. Black arrows show the water level of each survey year such as 2014 ~6.59 m, 2005 ~4.42 m and 2017~3.36 m, Ovals show regions of large recorded amplitudes caused by the erosion of the ironstone beds at both ends of the cliff face. The uppermost thin yellow line in each one of them is the free surface topography. Plotted depths are relative to the highest elevation on the line, at ~12 m, not relative to the topography. The solid black vertical line is the reference location at the center of the CMP. This is where the velocity profiles of Figure 14 are determined.



MHz datasets (Figures 17 (d), (e) and (f)), we consistently lose information as we go toward the south end where the land surface is closest to lake level.

As the frequencies of GPR data of 2014 and 2005 are increased to 200 MHz, the resolution increases, attenuation increases, and the depth of radar penetration decreases to 6 m (Figures 17(g and h). By examining the 200 MHz radar profiles of 2014, 2005 and 2017 in (Figures 17(g, h and i), it is interesting to find that, as the water rises, there is more attenuation of the radar signals. There is a large decrease in the amplitude of the 200 MHz data with increasing water level at depths greater than 2 m from 2014 through 2017. At depths less than  $\sim 1.8$  m, amplitudes remain  $\sim$ unchanged for all the three 200 MHz datasets. This again attests to the fact that, rock materials at shallow depths at the time of all three surveys are unsaturated and thus less conductive, giving fairly constant, large amplitudes.

### **3.2.1 Analysis of 2D models as a function of fresh and ground water distribution.**

There is good relation between GPR amplitude changes of 50 MHz, 100 MHz and 200 MHz data from 2014 to 2005 with the 2.21 m change in lake water level (Figures 17 (a), (b), (d), (e), (g) and (h)). However, there is an apparent inconsistency when compared to the amplitudes at the equivalent frequencies of the 2017 data. The lake level is highest in 2017 and we expect higher attenuation and a smaller depth of penetration of the GPR signal.

However, the 2017 GPR data has less attenuation and greater depth of penetration than the 2014 and 2005 data do (Figures 17(c), (f) and (i)). Consider the cause of this observation. Attenuation is a consequence of the electrical conductivity of the groundwater. Saturation of rock



by ground water increases the conductivity of the rock-water medium (1 mS/m to 3000 mS/m) as ions from dissolved minerals move freely in the pore spaces of the rocks to carry electrical current and this increased conductivity increases attenuation with a corresponding reduction in depth of

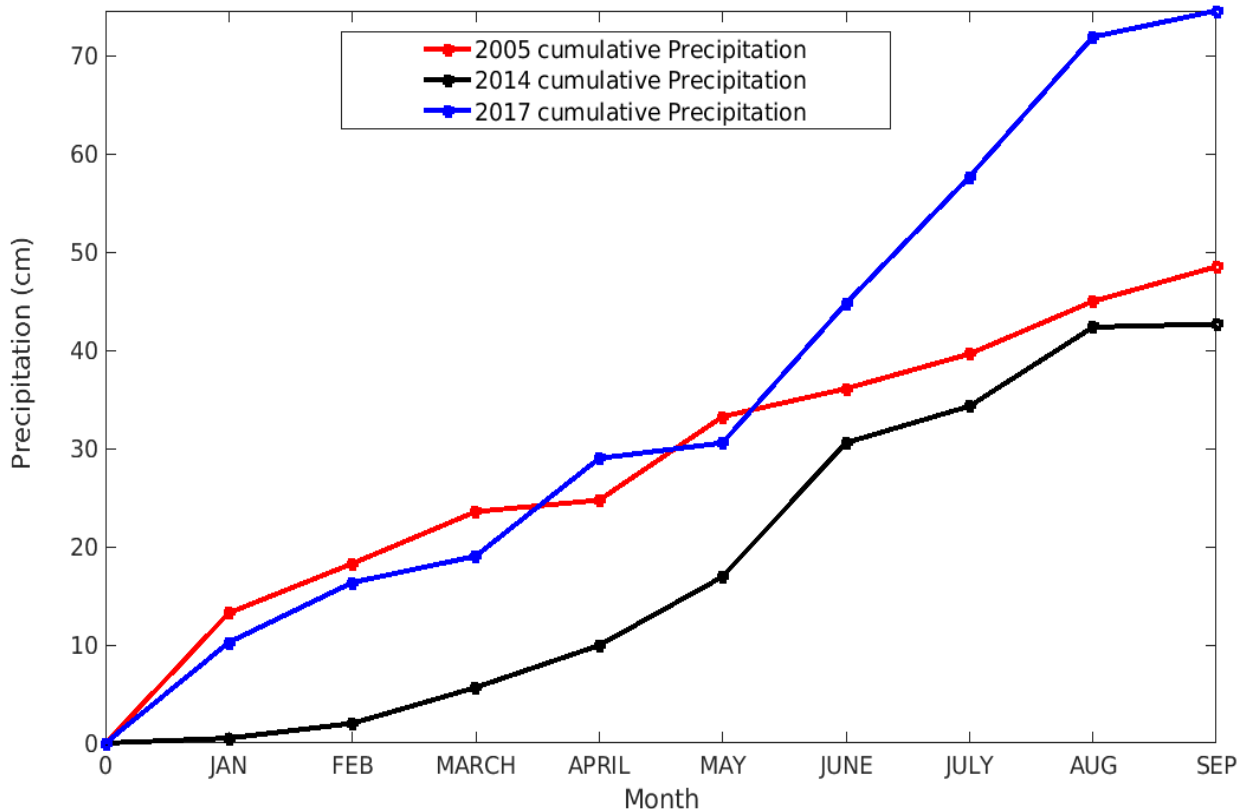


Figure 18. Cumulative precipitation of 2005, 2014 and 2017 prior to the day of GPR data collection. Of these 3 years, the least amount of rainfall 42.7 cm was recorded in 2014. 2005 had 48.53 cm; 2017 had 74.6 cm. All precipitation data are converted from inches to cm. Modified after DFW iWeatherNet, 2017.

penetration. However, water is not always as conductive as popularly assumed. Fresh water, such as rainwater, containing fewer dissolved ions, has very low conductivity of the order of  $\sim 0.5$  mS/m (e.g., van Dam, 2001). Figure 18 shows the accumulated amount of fresh water that was added to

the survey area from precipitation in each of the three years prior to the time GPR data were collected in those years. The least amount of accumulated rainfall (42.7 cm) was in 2014. 2005 had an intermediate amount (48.53 cm) and 2017 had the highest (74.6 cm).

Up until the end of May in 2005 and 2017, the site had fairly equal amounts of rainfall, but subsequent heavy rain from May to September in 2017 gave a 53.7% increase in cumulative precipitation compared to that of 2005, and 74.7% more than that recorded in 2014. The density of ground water at surface temperature (14.6°C) is 1.03 g/cm<sup>3</sup> (McGuire, 1998) and that of fresh water from precipitation is 1.0 g/cm<sup>3</sup> (Cohen, 1994). The density of water is affected by its temperature and its salinity. Since the surveys were done at nearly the same time of each year and at the same place, we assume a constant value for each of these determining factors.

With information about the additional fresh water from rainfall absorbed by the surveys site in 2017, it is not surprising to see large differences in the trend of the relationship between the water table position and attenuation. With fresh water being slightly less dense than the ground water (McGuire, 1998; Cohen, 1994), rainwater added to the survey site reduces the electrical conductivity (and hence reduces the GPR attenuation) at the water table.

During a prolonged rain, the ground water which contains free-moving ions in the pores spaces of the rocks will be replaced by freshwater which contains fewer ions even at depths as large as 8.5 m in the 2017 50 MHz data. This reduces the average conductivity of the rock and thereby increasing the depth of GPR penetration; Figures 17(c) and 17(f) show large amplitudes are recorded from greater depths in the 50 MHz data of 2017 where the lake water level is highest. Thus, a consequence is that the reflections from the deeper lithologic layers are less attenuated

than the same reflections in the corresponding 2005 and 2014 data. The fresh water-to-ground water interface is believed to exist at a depth less than 9 m even though it is not well defined in Figure 17 (c), presumably because of mixing of the rain-water and ground-water in a transition zone.

#### **3.2.1.1 Control of fresh and lake water distribution and visibility of GPR reflections by porosity.**

The depositional systems of the Cretaceous Woodbine Formation of Texas have been studied for their highly porous sandstones and potential for economic development (Main, 2006). As a vital aquifer in McLennan, Cooke and Red river counties, water produced from the Woodbine formation supplies municipal, industrial, domestic, livestock and small irrigations in many parts of North Texas (Ashworth and Hopkins, 1995).

Studies from wells drilled in the East Texas Oil Field show that the Woodbine reservoir sandstone at 4200 m depth has ~23% porosity (Sticklin, 2002). Research conducted in the Woodbine sandstone and aquifers in the North Texas area by Ashworth and Hopkins, (1995) and Brun et al., (2016) predicts 18% to 21% porosity. Hence, we assume the porosity of the rocks of the survey area to be ~0.2.

The depth extent of the unsaturated cliff face above the water table in each of the years GPR data were collected are known from our level and rod measurements. Figures 17 (a), (b) and (c) show GPR images that are consistent with the measured depths from the reference elevation at the highest point on the line down to the fully saturated water table in 2014, 2005 and 2017 of 6.59 m, 4.42 m and 3.36 m, respectively. With this information, and by assuming a typical porosity of

0.2, we can estimate the amount of precipitation required to raise the water table to the surface and thus, to flood the survey site. For example, the amount of rainfall that would saturate to the highest

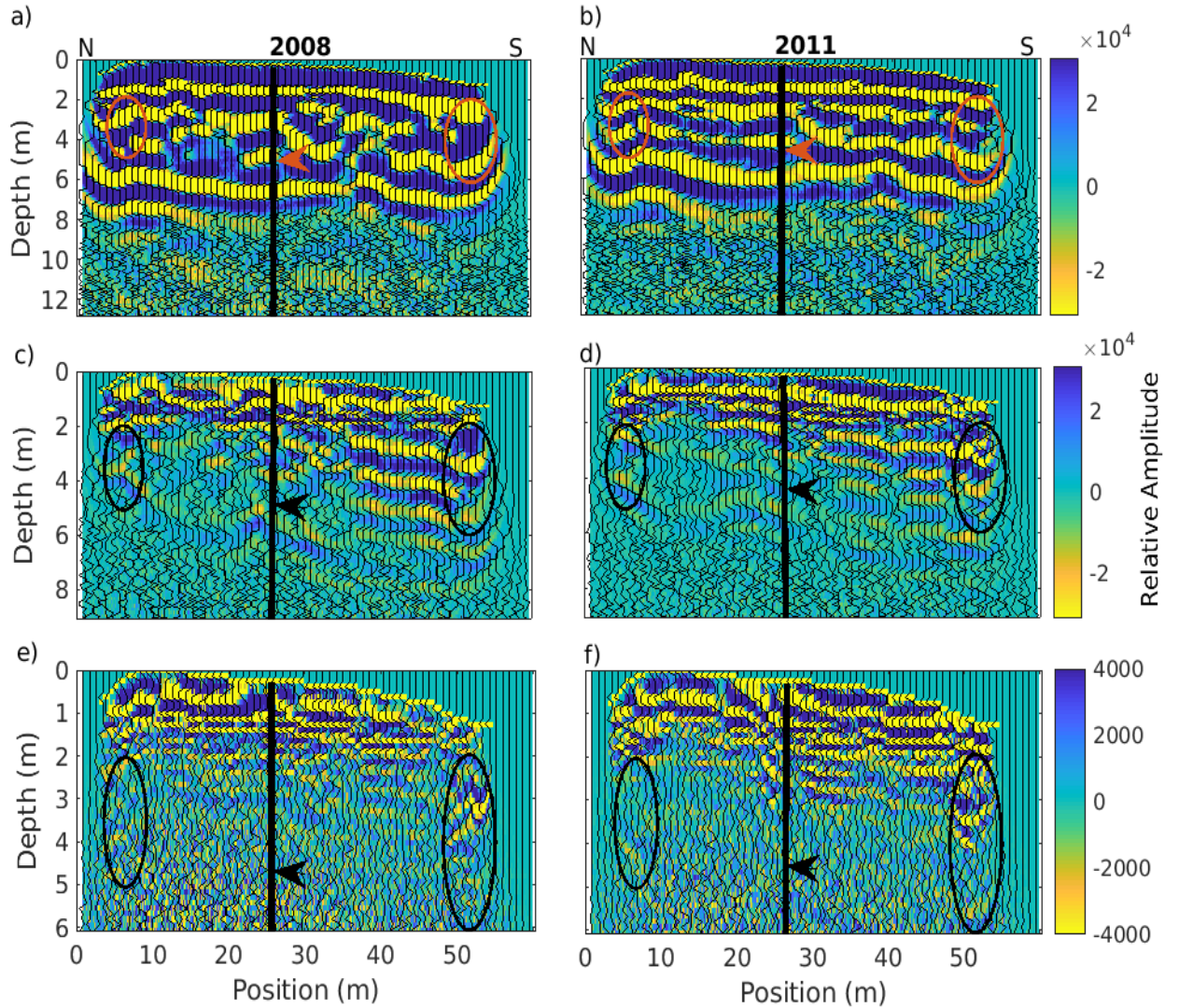


Figure 19. 50MHz, 100 MHz and 200 MHz matrix and wiggle profile plots of 2008 (a, c and e) and 2011(b, d and f) data showing the water table, the strength of attenuation and subsurface geologic features. All 50 MHz data (a and b) are plotted to a maximum depth of 13 m, 100 MHz (c and b) to a maximum depth of 9 m and the 200 MHz (e & f) to a maximum depth of 6.1 m. Traces are sampled at 0.125 m. Arrows show the water level of each year such as 2008 ~ 4.81m and 2011~ 4.46 m. Ovals show regions of large recorded amplitudes caused by the erosion of ironstone beds at both ends of the cliff face. The uppermost thin yellow line in each figure is the free surface topography. Plotted depths are relative to the highest elevation on the line, at ~12 m, not relative to the topography. The solid black vertical line is the reference location relative to the center of the CMP. This is where the velocity profiles of Figure 14 are determined.

point on the surface in 2014 is calculated as  $6.59 \text{ m} \times 0.2 = 131.8 \text{ cm}$ . Repeating this calculation for the 2005 and 2017 data gives 88.4 cm and 67.2 cm respectively.

The water table is deeper in 2014 than in 2017 (table 1). The volume of unsaturated rock pore space available to be filled with any additional water decreases, and the rate at which this happens, defines the saturation gradient of the rocks over years of changing water table. The complement of this process is also true; i.e., if we measure the amount of precipitation needed to raise (or lower) the water table through a given height increment, the porosity of the rock as a function of depth can be computed.

These calculations are necessarily very approximate as they are based on a static 1D model. The assumptions include homogeneity of connected porosity, a flat topographic surface, no lateral transport of water from the saturated subaerial rock into the lake, no evaporation, and that there is no artificial influence on the lake level generated by opening or closing the dam at the end of the lake during the measurement period.

### **3.2.2 Repeatability of data from years with small differences in lake level.**

The foregoing analysis of changes in GPR attenuation and amplitude with the rising water level makes a consistent story, except for the 2017 data, whose amplitude and attenuation abnormalities at depth are caused by the presence of additional fresh water. For consistency, it is important to repeat the analysis using GPR data collected in two other different years that have small difference in lake elevation and compare the results with those described in Chapter 3.2.1. With only 0.2 m difference in lake water elevation (Table 1), GPR data collected in 2008 and 2011

are appropriate to be used for the water table confirmation experiment. Figure 19 shows the 50, 100 and 200 MHz data from both years with almost equal water level.

The 50 MHz profiles of 2008 and 2011 (in Figures 19a and 19b) are nearly identical in terms of the depth of GPR penetration and the amplitudes at those depths, except for small incoherent features found at ~5 m depth in the 2008 data which are not seen in the 2011 data. The 100 MHz profiles are very similar. Amplitudes at 0 m to ~2 m depths are equally large in both 100 MHz profiles; for depths greater than 2 m, low amplitudes are seen at the south end of both 100 MHz Figures 19(c) and 19(d) where the water table is closer to the topographic surface. Large amplitudes are also recorded at the north end where the height of the cliff face above the water table, is larger than at the south end side making the rocks have lower average saturation. These observations are also similar in the 200 MHz profiles (Figures 19e and 19f). The amplitude changes in the 200 MHz data (Figures 19e and 19f) from north to south follow the same trend as found in the lower frequencies except that they have higher resolution and larger vertical magnification.

Comparing the 2008 and 2011 data (Figure 19) where the water levels are closer to each other, with that from 2014, 2005 and 2017 (Figure 17) data, it is concluded that the changing of the water level of the lake and the corresponding changes in the water table position, and hence the associated dielectric and conductive properties of the water, causes predictable distinctive, visible changes in GPR data amplitudes, attenuations and velocities.

### **3.3 Sensitivity of GPR to ironstone beds.**

Hematite is an iron oxide that is highly attenuating of electrical waves. Its typical resistivity ranges from  $\sim 3.5 \times 10^{-3} \Omega\text{m}$  to as large as  $\sim 3.5 \times 10^7 \Omega\text{m}$  (Kariya, and Shakland, 1983),

which can significantly affect radar signals. These effects are usually not associated with the electrical resistivity or permittivity of the hematite, but rather by its water retention (van Dam, 2001). A large part of the topographic surface of the survey site is in a layer containing red ironstone concretions (Figures 4, 10 and 20). However, the iron- rich layer has been eroded away at both ends of the cliff face. The electrical conductivity of the top, iron-containing, layer reduces the amplitude of all GPR reflections from deeper layers such as the water table. The data profiles show stronger reflections are recorded at the ends of the cliff face where the iron-rich layer is eroded off (see in the ovals in Figure 19c, 19d, 19e and 19f) as compared to signals collected at positions near the center, which lie beneath the beds with ironstone filled fractures (Figure 20).



Figure 20. Hand sample of an ironstone concretion from Unit 7. The dominant mineral is hematite which exhibits strong attenuation of electromagnetic waves.

## **CHAPTER 4**

### **DISCUSSION AND CONCLUSION**

#### **4.1 Discussion**

The unique data set available for this study consists of eight repetitions of a short GPR line recorded at times that correspond to different water table levels and different amounts of fresh (rain) water lying above the ground water. The surveys were conducted along a bluff at a lakeshore for which the lake surface elevations were accurately known; this, along with the exposed section supports the interpretations of the observations.

If the frequency-dependence of the GPR velocity is correctly estimated, including the contribution of the water distribution and properties, then the images of each boundary after migration will coincide across all frequencies. Despite giving many satisfactory results in this analysis, more complete models could be produced if 3D data were acquired; 3D GPR data volumes would lead to volumetric estimations of the available void space to be filled by additional fresh water.

As an analog of a reservoir rock, and as an aquifer, characterization and imaging of 2D and 3D features may be performed by velocity and attenuation tomography if more offsets were recorded; this would also facilitate analysis of multi-offset amplitudes as a function of reflection angle. This is left for a future project.



## **4.2 Conclusions**

GPR data recorded at any time contain the superimposed signatures of both the time-independent sedimentology and the time-dependent distribution of the water. Both the GPR velocities and attenuations are affected by the water distribution and chemistry. This allows identification of the parts of the data that contain information about the water content through both the related reflections, and the frequency-dependent attenuation. Fresh, low-density water with low ion content, such as rain, lies above higher-density, higher-ion-content ground water, and affects the GPR velocity similarly, but has significantly lower attenuation; this allows the underlying sedimentology to be imaged deeper, even though it is water saturated. A hematite-rich layer at the top of the exposed section reduces the GPR amplitudes except at the two ends of the survey line where it is eroded off, and thus facilitates stronger reflections from the deeper interfaces.

## APPENDIX A

### TIME TO DEPTH CONVERSION

GPR systems record the time for a radio wave to travel to a reflector surface and back. The depth to the target is calculated based on the velocity at which the wave travels to the target and back. The RMS velocities obtained from our velocity analysis are converted to interval velocities for the depth calculations. Depth is derived as:

$$D_i = \sum_i v_i T_i$$

where  $D_i$  is depth (m) to the bottom of layer  $i$ ,  $V$  is the interval velocity (m/ns) within layer  $i$ , and  $T$  is the one-way vertical travel time (ns) within it.

## APPENDIX B

### ESTIMATION OF ROCK POROSITY

The porosity of the rocks is estimated from the GPR data using Archie's first equation which gives the empirical quantitative relationship between porosity ( $\Phi$ ) and formation factor (F) as:

$$F = \Phi^{-m}$$

Where  $m$  is the exponent which increases with compaction, cementation and consolidation.

When the conductivity of the boundary layers is negligible, the equation above can be written as:

$$\Phi^m = \frac{\sigma_o}{\sigma_w}$$

where  $\sigma_o$  is the conductivity of the saturated rock,

$\sigma_w$  is the conductivity of the electrolyte (water).

## APPENDIX C

### GOVERNING EQUATION OF GPR VELOCITY

The velocity and attenuation of electromagnetic wave propagation through a material are heavily dependent on the composition and water content of that material (Gueguen and Palciauskas, 1994). The velocity of electromagnetic waves is given by

$$V_m = c / \{(\epsilon_r \mu_r / 2)[(1 + P^2) + 1]^{1/2}\},$$

where  $c$  = the speed of light in free space,  $\epsilon_r$  = the relative dielectric permittivity,  $\mu_r$  = the relative magnetic permeability (=1 for non-magnetic materials).  $P$  = the loss factor such that  $P = \sigma / \omega$  where  $\sigma$  = conductivity in (mS/m),  $\omega = 2\pi f$  where  $f$  is the frequency in Hz. The velocity of electromagnetic waves in low-loss materials ( $P \approx 0$ ) is reduced to  $v = c / \sqrt{\epsilon_r}$ .

Attenuation coefficient ( $\alpha$ ) is an important parameter that determines the maximum depth of GPR penetration in rocks and is given as (Reynolds, 2011);

$$\alpha = \omega \left\{ \left[ \frac{\mu \epsilon}{2} \right] \left[ \left( 1 + \frac{\sigma^2}{\omega^2 \epsilon^2} \right)^{1/2} \right] - 1 \right\}^{1/2}$$

where  $\omega = 2\pi f$  where  $f$  is frequency in Hz,  $\mu$  is the magnetic permeability ( $4\pi \times 10^{-7}$  H/m),  $\sigma$  is the bulk conductivity (S/m) at given frequency  $\omega$ .

## APPENDIX D

### 2D PROFILE IMAGES OF GPR DATA FROM OTHER YEARS

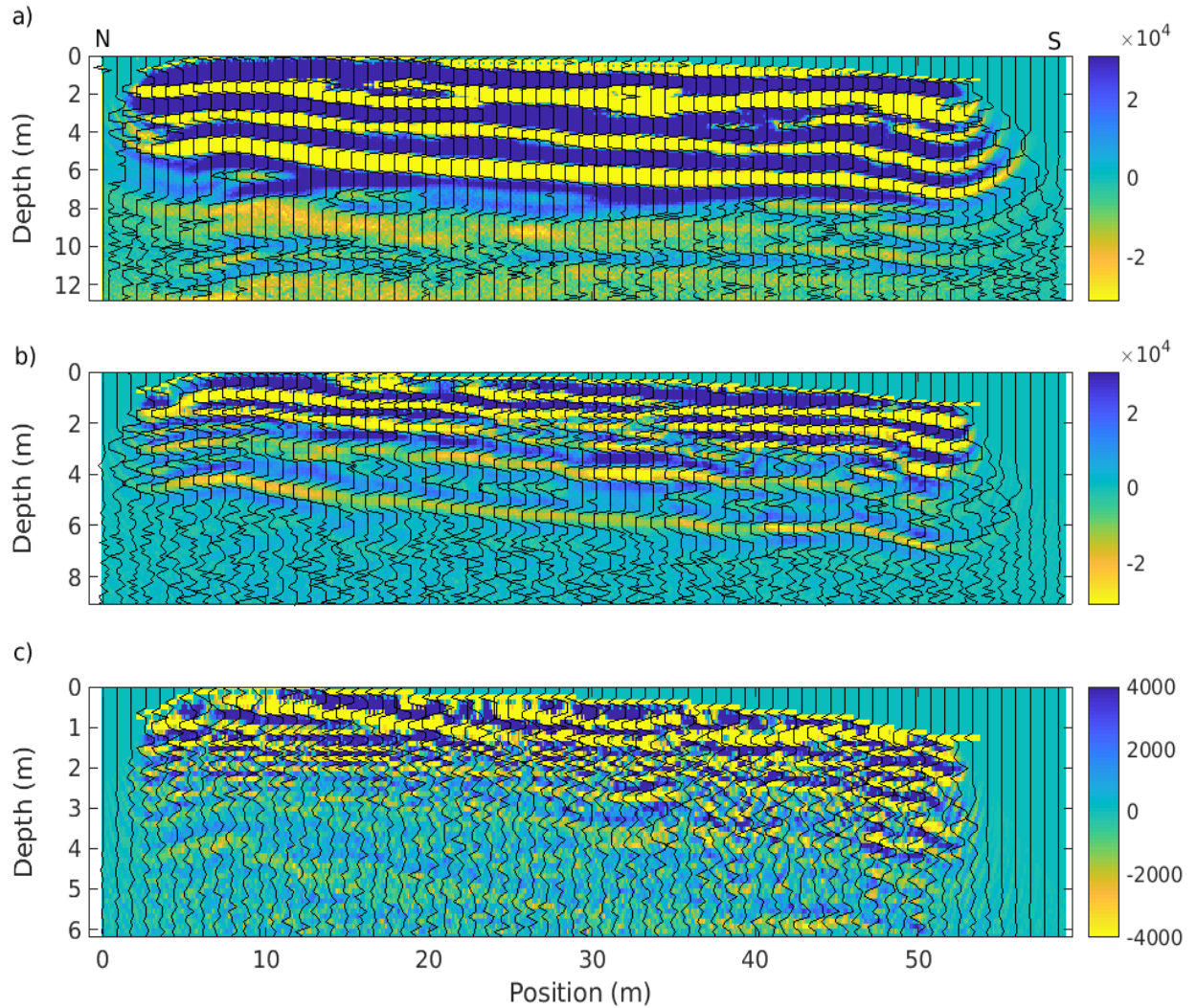


Figure 21. (a) 50MHz, (b) 100 MHz and (c) 200 MHz matrix and wiggle profile plots of 1998 data showing the strength of attenuation and subsurface geologic features. 50 MHz data (a) is plotted to a maximum depth of 13 m, 100 MHz (b) to a maximum depth of 9 m and the 200 MHz (c) to a maximum depth of 6.1 m. Traces are sampled at 0.125 m. Lake elevation at the time of data collection is 161.7 m. The uppermost thin yellow line in each figure is the free surface topography. Plotted depths are relative to the highest elevation on the line, at  $\sim 12$  m, not relative to the topography.

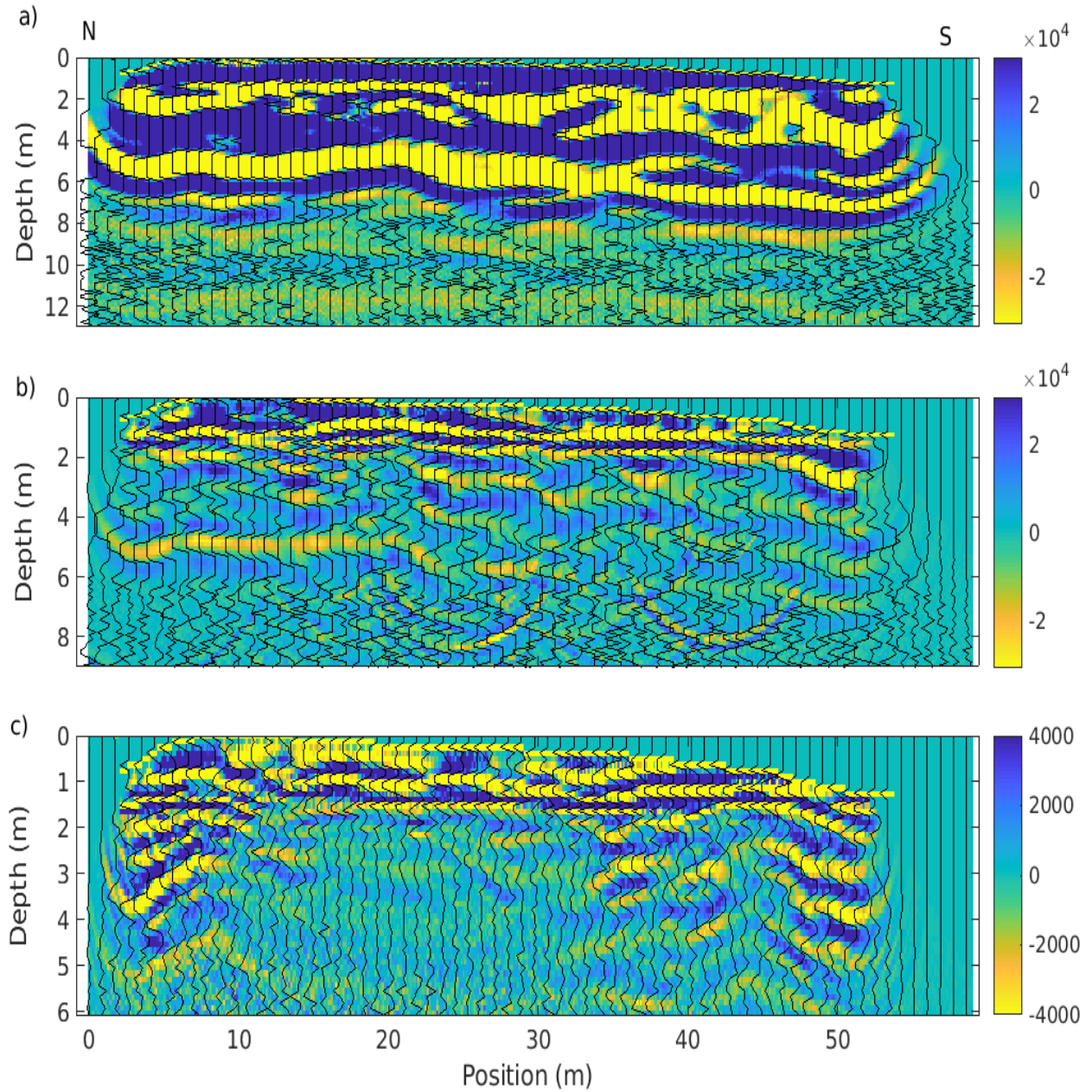


Figure 22. (a) 50MHz, (b) 100 MHz and (c) 200 MHz matrix and wiggle profile plots of 2000 data showing the strength of attenuation and subsurface geologic features. 50 MHz data (a) is plotted to a maximum depth of 13 m, 100 MHz (b) to a maximum depth of 9 m and the 200 MHz (c) to a maximum depth of 6.1 m. Traces are sampled at 0.125 m. Lake elevation at the time of data collection is 159.57 m. The uppermost thin yellow line in each figure is the free surface topography. Plotted depths are relative to the highest elevation on the line, at ~12 m, not relative to the topography.



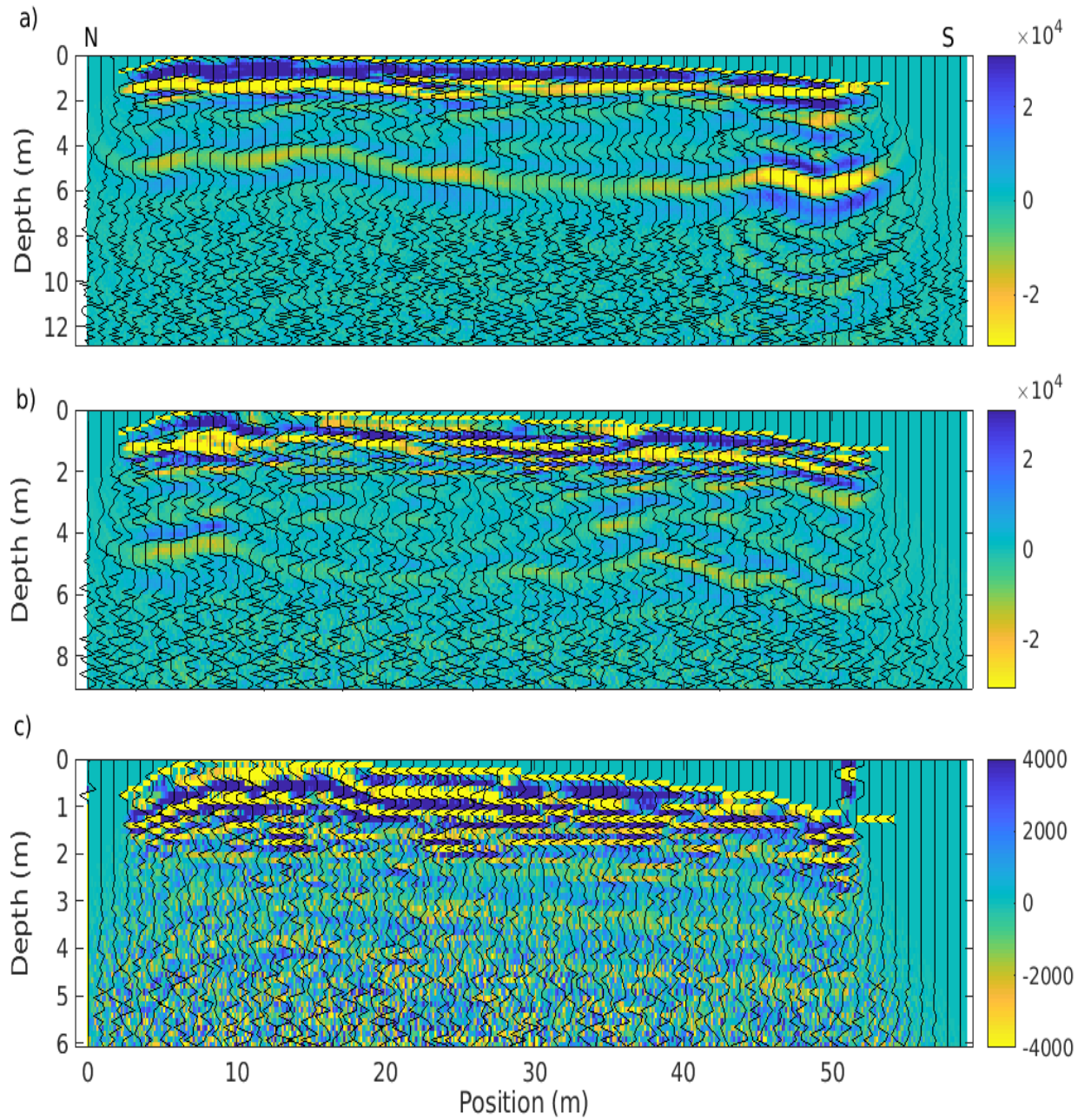


Figure 23. (a) 50MHz, (b) 100 MHz and (c) 200 MHz matrix and wiggle profile plots of 2002 data showing the strength of attenuation and subsurface geologic features. 50 MHz data (a) is plotted to a maximum depth of 13 m, 100 MHz (b) to a maximum depth of 9 m and the 200 MHz (c) to a maximum depth of 6.1 m. Traces are sampled at 0.125 m. Lake elevation at the time of data collection is 162.2 m. The uppermost thin yellow line in each figure is the free surface topography. Plotted depths are relative to the highest elevation on the line, at ~12 m, not relative to the topography.

## REFERENCES

- Annan, A. P., 2005, Ground-penetrating radar: *in* Butler, D. K., Ed., Near surface Geophysics: Investigations in Geophysics 13, SEG, 357-436.
- Ashworth T. B. and Hopkins J., 1995, Aquifers of Texas, Texas Water Development board Report 345., 42-44.
- Bentley, L.R. and Trenholm N. M., 2002, The Accuracy of Water Table Elevation Estimates determined from Ground Penetrating Radar Data. Journal of Environmental & Engineering Geophysics, no. 3, 37-53.
- Bergquist, H. R., 1949, Geology of the Woodbine formation of Cooke, Grayson, and Fannin counties, U.S. Geological Survey, no. 5, 19-34.
- Bradford, J. H., 2007, Frequency-dependent attenuation analysis of ground-penetrating radar data: Geophysics, 72, no. 3, J7-J16.
- Brun B. et al., 2016. Groundwater quality flow and contributions to surface water. Texas Aquifers Study., Texas Water Development Board, 249-254.
- Bunge, R.J., 2007, Woodbine Formation sandstone reservoir prediction and variability, Polk and Tyler counties, Texas: Gulf Coast Association of Geological Societies Transactions, 57, 77-98.
- Cai, J., and G. A. McMechan, 1995, Ray-based synthesis of bistatic ground penetrating radar profiles: Geophysics, 60, 87-96.
- Cassidy, N. J., 2008, GPR attenuation and scattering in a mature hydrocarbon spill: A modeling study: Vadose Zone Journal, 7, 140-159.
- Cohen, P., and G. Saul, 1994, Chemistry; A contemporary Approach: AMSCO School Publications Incorporated, New York., no. 18, 99-112.
- Davis, J. L., and A. P. Annan, 1989, Ground-penetrating radar for high-resolution mapping of soil and rock stratigraphy: Geophysical Prospecting, 37, 531-551.
- Dodge, C. F., 1969. Stratigraphy of the Woodbine Formation in the Arlington Area, Tarrant County, Texas Cretaceous Sediments; Geolex-Lewisville Publications, 2, 66-73.
- Doolittle J.A., Jenkinson B., Hopkins D., Ulmer M. and Tuttle W., 2005, Hydropedological investigations with Ground-Penetrating Radar: Estimating water-table depths and local ground-water flow pattern in areas of coarse-textured soils, Geoderma 131, 317-329.



- Epili, D., and G. A. McMechan, 1996, Implementation of 3-D pre-stack Kirchhoff migration, with application to data from the Ouachita frontal thrust zone: *Geophysics*, 61, no. 3, 10-32.
- Fisher, E., G. A. McMechan, P. Annan, and S. Cosway, 1992a, Acquisition and processing of wide-aperture ground-penetrating radar data: *Geophysics*, 57, 495-504.
- Fisher, E., G. A. McMechan, P. Annan, and S. Cosway, 1992b, Examples of reverse-time migration of single-channel, ground-penetrating radar profiles: *Geophysics*, 57, no. 2, 577-586.
- Fort Worth Army Corps of Engineers, 2017. GPVT2 ELEV. OBS. FT-NGVD, INST-VAL. 24-hour Lake records of the Grapevine Lake, <http://www.swf-wc.usace.army.mil/reports/query/gpvt2.200022.html>
- Grote, K., C. Anger, B. Kelly, S. Hubbard, Y. Rubin, 2010, Characterization of Soil Water Content Variability and Soil Texture using GPR Groundwave Techniques water content changes: *SAGEEP*, 260-263, / <http://doi.org/10.2113/JEEEG15.93-046>
- Grunewald, E., 2017, Analysis of time-shift distributions between GPR records with scattered events to detect fluctuations of water table: *SAGEEP*, 260-263, /<http://doi.org/10.4133/SAGEEP 30-014>.
- Gueguen, Y. and Palciauskas V., 1994, *Introduction to the Physics of Rocks*, Princeton University press, 41:183-209.
- Harbi, H. and G. A. McMechan, 2011, 3D Reservoir Analog Characterization using GPR: *Geophysics*, no., 12-17.
- Hundnall, J. S. and R.W. Eaton, 1968, Geology of Woodbine Formation in East Texas Oil Field and Related Areas: *AAPG Bulletin*, no. 3, 532-533.
- Igel, J., S. Stadler, T. Guenther, 2016, High-resolution investigation of the capillary transition zone and it's influence on GPR signatures: *SAGEEP*, 260-263, / <http://doi.org/10.4133/SAGEEP.29-046>
- iWeatherNet, 2017, Monthly and Annual Total Precipitation of Grapevine Dam, Texas, NowData, NOAA online weather data, <https://www.iweather.net/texas-dfw-weather-records>.
- Kariya, K. A., and Shakland, T. J., 1983, Electrical conductivity of dry lower crustal rocks, *Geophysics* 48, 52-61.

- Klotzsche A., L. Lärm, L. Weihermüller, J. Vanderborght, H. Vereecken, J. Kruk, 2018, Time-lapse horizontal borehole GPR measurements to investigate spatial and temporal soil-water content changes: SAGEEP, 260-263, / <http://doi.org/10.1190/sagem201843.1> 29-045
- Kowalczyk, S., A. Lejzerowicz, B. Kowalczyk, 2018, Groundwater table level changes based on ground penetrating radar images: a case study. Faculty of Geology, University of Warsaw, *Zwirki I Wigury* 93, 02-089.
- Kowalsky, M. B., S. Finsterle, J. Peterson, S. Hubbard, Y. Rubin, E. Majer, A. Ward, and G. Gee, 2005, Estimation of field-scale soil hydraulic and dielectric parameters through joint inversion of GPR and hydrological data: *Water Resources Research*, no. 41, 1-19.
- Lee, K, X. Zeng, G. A. McMechan, C. Howell Jr., J. Bhattacharya, F. Marcy, and C. Olariu, 2005, A ground-penetrating radar survey of a delta-front reservoir analog in the Wall Creek Member, Frontier Formation, Wyoming: *American Association of Petroleum Geologists Bulletin*, 89, 1139-1155.
- Lee, Y.-N., 1997, Bird and Dinosaur footprints in the Woodbine Formation (Cenomanian), Texas. *Cretaceous Research*, 18, 849-864.
- Liu, L., 2006, Fracture characterization using borehole radar: Numerical modeling: *Water, Air, and Soil Pollution: Focus*, 6, 17-34.
- Main, J. D., 2006, Paleoenvironments and Paleocology of the Cenomanian Woodbine Formation of Texas; *Paleobiography of the Hadrosaurs (Dinosauria: Ornithischia)*, UMI microform 1429361, 53-65.
- McGuire, T., 1998, Earth science: The physical setting, *The Physics Factbook*; 123. AMSCO school publications incorporated, New York, no 4, 11-123.
- Nabighian, M. N., 1988, Electromagnetic methods in Applied Geophysics: *Society of Exploration Geophysicists, Investigations in Geophysics No. 3*, v 1, 13 – 48.
- Oliver, W. B., 1971, Depositional systems in the Woodbine Formation (Upper Cretaceous) Northeast Texas. *Bureau of Economic Geology* 73, 14-26.
- Parsekian, A. D., 2018, Inverse Methods of Improve Accuracy of Water Content Estimates from Multi-offset GPR: SAGEEP, 260-263, / <http://doi.org/10.2113/JEEG23.3.349>
- Reynolds, J. M., 2011, *An Introduction to Applied and Environmental Geophysics*, John Wiley & Sons, 535-548.

- Sambhaji, P. A., 2016, Ground Penetrating Radar, Principles and Components, Advanced Geospatial Technology: GIS no. 2, 1519, 14.
- Scheihing, H. M., and J. A. Lorsche, 1995, Woodbine reservoir sandstones in Denton and Tarrant counties, Texas., Geological field trip guide, SPE annual technical conference and exhibition, ARCO exploration and production technology, 4-10, 22-63.
- Sege, M. A., and Nashait, A. F., 2011, Detection of water-table by using ground penetrating radar: Eng. & Tech. Journal, 29, 555-558.
- Sensors and Software<sup>®</sup>, 1996, 2D Ray Trace Modelling, User's Guide, Version 1.0: Technical Manual 26, PulseEKKO Inc., 14-25.
- Stricklin F. L. Jr., 2002, Evolution and high dissolution porosity of Woodbine Sandstones in a slope submarine fan, Double A Wells Field, Polk County, Texas- A Deep Water Gulf of Mexico Model Onshore: Wilcox Exploration Enterprises, 13-27.
- Taherian, M. R., W. E. Kenyon, and K. A. Safinya, 1990, Measurement of dielectric response of water-saturation rocks: Geophysics, 55, no. 6, 1530-1541.
- van Dam, R. L., 2001, Causes of ground-penetrating radar reflections in sediment: PhD thesis, Vrije University, Amsterdam; 8-95.
- Xu, T., and G. A. McMechan, 1997, GPR attenuation and its numerical simulation in 2.5 dimensions: Geophysics, 62, no. 4, 403-414.

## **BIOGRAPHICAL SKETCH**

Samuel Kwaku Amankwaa (Sam Amankwaa) was born on June 15, 1988, to George and Theresa Amankwaa in Tepa, Ghana. After gaining quality high school education from Opoku Ware School, he attended the University of Ghana (UG) where he obtained a bachelor's degree in Geology (Honors) in 2012. At UG, he completed a thesis research on the Petrography and Geochemistry of the Elmina Sandstone Formation. As an undergraduate, he was offered an internship opportunity by the Ghana Geological Survey Authority where he worked on rocks samples from the Sekondian Series containing the Ajua shales, a real reservoir rock for the Jubilee producing fields in the offshore Gulf of Guinea. By so doing, he gained skills in professional Geochemistry such as XRF and LOI tests and drew reasonable interpretation from the results. Prior to this, he acquired fundamental knowledge of geological field mapping, subsurface mapping and sequence stratigraphic analysis during the summers of 2009 and 2010 at the Workers College of the University of Ghana.

Sam began his studies in the Geosciences department at The University of Texas at Dallas (UTD) in 2016. He is an active student member of the Society of Exploration Geophysicist (SEG), the American Association of Petroleum Geologists (AAPG), Geological Society of America (GSA) and the UTD GeoClub. He presented the original research work of this thesis at conferences of these organizations between the years of 2017 and 2019. His passion for petroleum geosciences and his hard work in the area got him selected as a member of the team to represent The University of Texas at Dallas (UTD) for the Imperial Barrel Award (IBA) program. The team performed excellently and was awarded third place in the 2018 (AAPG) IBA, Southwestern section. He is a Permanent Resident of the United States and is anticipated to become a citizen in 2019.

## **CURRICULUM VITAE**

**Samuel Kwaku Amankwaa**

### **EDUCATION**

**University of Texas, Dallas**—MS. Geosciences

Graduation —May, 2019

**University of Ghana, Accra - Ghana** —BS. Geology

Graduation — November, 2012

### **EXPERIENCE**

**Geophysical Consortium -- Geosciences Department, UTD** --Richardson, TX.

Research Assistant in Geophysics

Jan 2016 - May 2019

- Competently managed large geophysical dataset for thesis and reduced time and cost of processing and research by 4%.
- Used Kingdom Suite and Paradigm17 to analyze 9 well logs and interpret 215 seismic lines of the Taranaki Basin -New Zealand and drew good prospects for UT Dallas IBA team- 2018.
- Analyzed water table movement near the Grapevine Lake, Texas- U.S.A over the past 19 years to document a previously unrecognized relation between the lake level and GPR attenuation for research purposes.

**AAPG Imperial Barrel Award Program**

Southwestern Section

Team Member

Jan 2018 - March 2018

- Worked with team to analyze assigned basin
- Assessed hydrocarbon potential, systems, plays and prospect.

- Identified essential elements of source, migration, seal and reservoir.
- Interpreted seismic, well logs and geologic data sets using IHS Kingdom
- Performed risk analyses on assigned basin.
- Presented and demonstrated results to industry professionals.

### **Ghana Geological Survey Department, Accra, Ghana**

Geology Intern

May 2011—Aug 2011

- Mapped mineral prospects by constructing and analyzing cross-sections, geologic maps, well logs, and production reports using Petra, ArcGIS, Opendtect and Agisoft.
- Provided technical support to interdisciplinary team comprising of Geologists and Engineers.
- Performed onsite tool preparation of measurement/logging probes and computed related software.

### **AWARDS**

- 3rd Place - AAPG Regional Imperial Barrel Award, Regional, Texas Section 2018.
- Stafford Excellence Scholarship. 2017 spring
- Best Graduate Student in the Geology of Texas/Permian Basin/ DFW 2017 spring

### **LANGUAGES**

English, French and Asante Twi

### **SHORT COURSES AND WORKSHOPS TAKEN**

- Workshop on Permian Basin Crustal Structure (Pioneer Natural resources, UTD, UTEP), April, 2018.

- Introduction to 3D seismic interpretation with Paradigm 17 (Pioneer Natural Resources), January, 2018.
- Integrated Basin and Play Analysis (ExxonMobil) AAPG/SEG Expo, September, 2016, 2018.
- 3D Seismic Attributes to Define Structure and Stratigraphy AAPG/SEG Expo. March, 2016.